

Energy Advances

Accepted Manuscript

This article can be cited before page numbers have been issued, to do this please use: S. Mandal, V. K. Pillai, M. Ranjana, T. Nair, J. Bhagavathsingh, S. L. Grage, X. Peng, J. W. Kang, D. Liepmann, A. Kannan, V. THAVASI and V. Renugopalakrishnan, *Energy Adv.*, 2024, DOI: 10.1039/D4YA00217B.



This is an Accepted Manuscript, which has been through the Royal Society of Chemistry peer review process and has been accepted for publication.

Accepted Manuscripts are published online shortly after acceptance, before technical editing, formatting and proof reading. Using this free service, authors can make their results available to the community, in citable form, before we publish the edited article. We will replace this Accepted Manuscript with the edited and formatted Advance Article as soon as it is available.

You can find more information about Accepted Manuscripts in the [Information for Authors](#).

Please note that technical editing may introduce minor changes to the text and/or graphics, which may alter content. The journal's standard [Terms & Conditions](#) and the [Ethical guidelines](#) still apply. In no event shall the Royal Society of Chemistry be held responsible for any errors or omissions in this Accepted Manuscript or any consequences arising from the use of any information it contains.

Manuscript ID: YA-ART-04-2024-000217View Article Online
DOI: 10.1039/D4YA00217B**TITLE: Van der Waal Gap modulation of Graphene oxide through Mono-Boc ethylenediamine Anchoring for Li-ion Batteries**

Sneha Mandal,¹ Vijayamohan K. Pillai,^{1*} Mano Ranjana Ponraj,² Thushara Nair,² Jebasingh Bhagavathsingh^{2*} Stephan L. Grage,³ Xihong Peng,⁴ Jeon Woog Kang,⁵ Dorian Liepmann,⁶ Arunachala Nadar Mada Kannan,⁷ Velmurugan Thavasi,⁸ Venkatasen Renugopalakrishnan⁹

1. Department of Chemistry, Indian Institute of Science Education and Research (IISER), Tirupati, Andhra Pradesh 517507, India.
2. Department of Applied Chemistry, Karunya Institute of Technology and Sciences, Coimbatore, Tamil Nadu 641114, India
3. Karlsruhe Institute of Technology, Institute of Biological Interfaces IBG-2, P.O. Box 3640, 76021 Karlsruhe, Germany
4. College of Integrative Sciences and Arts, Arizona State University, Mesa, AZ 85212, USA.
5. Laser Biomedical Research Centre, G. R. Harrison Spectroscopy Laboratory, Massachusetts Institute of Technology, Cambridge, Massachusetts 02139, United States
6. Department of Bioengineering, 80 Hearst Memorial Mining Bldg., University of California, Berkeley, CA 94720
7. The Polytechnic School, Ira A. Fulton Schools of Engineering, Arizona State University, Mesa, AZ 85212, USA
8. Center for Quantum Research and Technology, The University of Oklahoma, 440 W. Brooks Street, Norman, OK 73019, USA
9. Department of Chemistry, Northeastern University, Boston Children's Hospital, Harvard Medical School, Boston, MGB Center for COVID Innovation, MA 02115, USA

Corresponding Authors: vijay@iisertirupati.ac.in and jebasinghb@karunya.edu

The data availability statement is given below with the data rights to the responsible person whose email is highlighted.

10. **Synthesis of Materials**- Dr. Jebasingh Bhagavathsingh, Mano Ranjana Ponraj, Thushara Nair. Department of Applied Chemistry, Karunya Institute of Technology and Sciences, Coimbatore, Tamil Nadu 641114, India. jebasinghb@karunya.edu
11. **Solid-state NMR**- Dr. Stephan L Grage. Karlsruhe Institute of Technology, Institute of Biological Interfaces IBG-2, P.O. Box 3640, 76021 Karlsruhe, Germany stephan.grage@kit.edu
12. **Density functional theory**- Dr. Xihong Peng. College of Integrative Sciences and Arts, Arizona State University, Mesa, AZ 85212, USA. xihong.peng@asu.edu



13. **Raman studies-** Jeon Woog Kang, Laser Biomedical Research Centre, **G. R. Harrison** Spectroscopy Laboratory, Massachusetts Institute of Technology, Cambridge, Massachusetts 02139, United States, jwkang76@mit.edu
14. **Electrochemical studies, FT-IR, Powder XRD, Post-mortem analysis-** Prof. Vijayamohan K. Pillai, Sneha Mandal. Department of Chemistry, Indian Institute of Science Education and Research (IISER), Tirupati, Andhra Pradesh 517507, India. vijay@iisertirupati.ac.in
15. **SEM, AFM-** Prof. Renugopalakrishnan Venkatasana, Department of Chemistry, Northeastern University, Boston Children's Hospital, Harvard Medical School, Boston, MGB Center for COVID Innovation, MA 02115, USA. v.renugopalakrishnan@northeastern.edu

[View Article Online](#)

DOI: 10.1039/D4TA00217B



Van der Waals Gap modulation of Graphene oxide through Mono-Boc ethylenediamine Anchoring for Superior Li-ion Batteries

View Article Online
DOI: 10.1039/D4YA00217B

Sneha Mandal,¹ Vijayamohan K. Pillai,^{1*} Mano Ranjana Ponraj,² Thushara Nair,² Jebasingh Bhagavathsingh^{2*} Stephan L. Grage,³ Xihong Peng,⁴ Jeon Woog Kang,⁵ Dorian Liepmann,⁶ Arunachala Nadar Mada Kannan,⁷ Velmurugan Thavasi,⁸ Venkatasen Renugopalakrishnan⁹

1. Department of Chemistry, Indian Institute of Science Education and Research (IISER), Tirupati, Andhra Pradesh 517507, India.
2. Department of Applied Chemistry, Karunya Institute of Technology and Sciences, Coimbatore, Tamil Nadu 641114, India
3. Karlsruhe Institute of Technology, Institute of Biological Interfaces IBG-2, P.O. Box 3640, 76021 Karlsruhe, Germany
4. College of Integrative Sciences and Arts, Arizona State University, Mesa, AZ 85212, USA.
5. Laser Biomedical Research Centre, G. R. Harrison Spectroscopy Laboratory, Massachusetts Institute of Technology, Cambridge, Massachusetts 02139, United States
6. Department of Bioengineering, 80 Hearst Memorial Mining Bldg., University of California, Berkeley, CA 94720
7. The Polytechnic School, Ira A. Fulton Schools of Engineering, Arizona State University, Mesa, AZ 85212, USA
8. Center for Quantum Research and Technology, The University of Oklahoma, 440 W. Brooks Street, Norman, OK 73019, USA
9. Department of Chemistry, Northeastern University, Boston Children's Hospital, Harvard Medical School, Boston, MGB Center for COVID Innovation, MA 02115, USA

Corresponding Authors: vijay@iisertirupati.ac.in and jebasinghb@karunya.edu



Abstract

View Article Online
DOI: 10.1039/D4YA00217B

Li-ion batteries stand out among energy storage systems due to their higher energy and power density, cycle life, and high-rate performance. Development of advanced, high-capacity anodes is essential for enhancing their performance, safety, and durability, and recently, two-dimensional materials have garnered extensive attention in this regard due to distinct properties, particularly their ability to modulate Van der Waal gap through intercalation. We have synthesised a crystalline covalently intercalated selectively protected mono-Boc-ethylenediamine into graphene oxide interlayer galleries (GO-EnBoc) via the epoxide ring opening, forming an amino alcohol moiety. This creates three coordination sites for Li ions exchange on the graphene oxide nanosheets' surface. Consequently, the interlayer *d*-spacing expands from 8.47 Å to 13.17 Å, as anticipated. When explored as an anode (Li-GO-En-Boc) show a significant enhancement in the stable and reversible capacity of 270 mA h g⁻¹ at a current density of 25 mA g⁻¹ compared to GO 80 mAh g⁻¹, without compromising the mechanical or chemical stability. Through ¹³C, ⁷Li and ⁶Li MAS NMR, XPS, IR, Raman microscopy, and density functional theory (DFT) calculations, we confirm the positioning of Li⁺ ions at multiple sites of the interlayer gallery, which enhances the electrochemical performance. Our findings suggest that these novel systematically modulated Van der Waal gap GO-engineered materials hold promise as efficient anodes for Li-ion batteries.

Keywords: 2D Materials, Van der Waal gap modulation, Intercalation, Interlayer *d*-spacing, Energy Storage, Molecular Engineering, LIBs.



1. Introduction

The current era is witnessing tremendous technological advances focused on improved energy storage and carbon neutrality for sustainability, as demonstrated by modern and futuristic innovative Li-ion batteries (LIBs). The societal transformation brought by these batteries from being a household item to portable electronics and more recently transportation and grid storage has brought a renaissance in the energy sector. Electric vehicles, from scooters to airplanes, require high performance energy storage, and intermittent energy sources from solar panels and wind farms require high-quality, secured storage with maximum energy efficiency and minimum loss.¹⁻⁴ Li-ion batteries (LIBs) being one of the most mature battery technologies in the commercial sector, still require better materials in terms of safety, stability, and cost compatibility.⁵⁻⁷ For example, a low-cost, cobalt-free cathode with excellent performance has recently been reported, and similar innovations abound.⁸ Lithium metal anode is considered as one of the most promising candidates for high energy and power density batteries due to its highest theoretical specific capacity (3860 mAhg⁻¹), high voltage, and highest redox potential (-3.04 V vs SHE). Furthermore, the small size of Li⁺ ion (76 pm) enables easy intercalation and deintercalation into the host structure during charge/discharge, as well as cyclic stability with excellent coulombic efficiency.^{9,10}

The search for better anode materials that are safer and more stable than pure Li metal led to the discovery of several alloy-based composites such as Si-Li and Sn-Li but these are not suitable for operation in batteries due to their large volume change upon lithiation and subsequent disintegration.¹¹⁻¹³ Of all materials, carbon-based anodes are more promising, primarily because of high reversibility, longer stability, good capacity (372 mAhg⁻¹), excellent capacity retention and low intercalation potential (~0 V vs Li/Li⁺). However, these materials have several limitations, including structural inhomogeneity, inadequate amount of intercalated Li⁺ ions, and poor thermal and electrical properties.^{14,15} In this context, graphene-based



materials have a promising future because of their large surface area ($2630 \text{ m}^2\text{g}^{-1}$), electron mobility ($15,000 \text{ cm}^2\text{V}^{-1}\text{s}^{-1}$), and short diffusion length of Li^+ ($\sim 30 \text{ }\mu\text{m}$) as well as their highly porous structure. Therefore, graphene is considered an interesting flexible material for superior performance of lithium-ion batteries (LIBs) because, in addition to flammability retardation it can enhance the battery capacity, efficiency, energy density, life cycle.¹⁶⁻¹⁸ Some of the limitations of these materials can also be alleviated by precisely modulating the interlayer d -spacing (van der Waal gap engineering), by surface functionalization.^{19,20} This also enables the formation of a continuous 2D/3D conducting network formed by graphene, stacked laterally and vertically thus effectively enhancing the electron and ion transport across the scaffolding, which in principle could improve the rate capability due to faster kinetics at the electrode-electrolyte interface.^{21,22} Consequently, graphene oxide (GO) and its surface-engineered variants, with numerous functional groups (e.g., hydroxyl, carboxyl, and epoxy) on their surfaces, especially at the basal planes where organic moieties can be grafted through chemical reactions with the functional groups, have attracted great interest in the development of rechargeable batteries.^{23,24} There are several reports on the challenges for the deposition of Li^+ on the surface of graphene and graphite through intercalation.^{14,25} For example, Lee *et al.* have synthesized Angstrom-level d -spacing (7-13 Å) control of graphite oxide using α , ω -diamino organic fillers for high-rate lithium storage.²⁶ Hyungsub *et al.* have synthesized the Janus nanostructures decorated with Fe_3O_4 nanoparticles and polydopamine on each side of graphene oxide with an interlayer spacing of 14.4 Å for LIBs.²⁷ Zhao *et al.* have synthesized Graphene oxide grafting naphthoquinone derivative for ZIBs.²⁸ Biradar *et al.* synthesised Bio-inspired adenine-benzoquinone-adenine pillar grafted graphene oxide materials with an interlayer spacing of 3.5 Å for supercapacitor application.²⁹ Gao *et al.* synthesised Stable metal anodes enabled by a labile organic molecule bonded to a reduced graphene oxide aerogel.³⁰ Banerjee *et al.* synthesised 1-Aza-15-Crown-5 Functionalized Graphene Oxide for 2D Graphene-Based

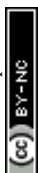
View Article Online
DOI: 10.1039/D4TA00217B



Li⁺-ion Conductor.³¹ However, some of these materials suffer from sluggish kinetics, and undesirable SEI layer formation, capacity fading and redox changes on Fe can potentially be difficult to control as a parasitic reaction. Moreover, none of the above works shows systematic modulation of the Van der Waal gap of GO without reducing it to rGO, by covalent grafting with selective functionalization to a structure-stable material to improve the kinetics, which enables faster mobility of Li-ions during charge/discharge processes.

Here, we report such an unprecedented strategy of intercalation of selectively mono tert-butyloxycarbonyl-protected ethylenediamine (EnBoc) in the GO basal planes with the enhancement of interlayer *d*-spacing (13.17 Å) as compared to GO (8.47 Å) without reducing it to rGO. The intercalation of EnBoc on the surface of GO enhances the interlayer spacing due to the covalent conjugation through the ring opening of epoxide by the nucleophilic attack of the primary amine. In the case of Lithiation to the enhanced *d*-spacing, it is known that the Lithium ions coordinate with the functionalized heteroatoms such as nitrogen and oxygen to form ternary complexes with the intercalant and GO basal planes.¹² By leveraging the intercalation of graphene oxide with appropriate organic molecules such as EnBoc in the design of the electrode, it is possible to covalently cross-link between amine functional groups and surface oxide groups on basal planes of GO to enhance porous nature, crystallinity, extended conjugation throughout the framework and most importantly being enriched with lithium-ion exchangeable sites that accelerate the intercalation of lithium ions in the pores of the material, and mechanical properties in a more robust manner compared to that of pristine GO. Both our interlayer spacing (13.17 Å) and diffusion coefficient (5.78×10^{-14}) values are much better than the values so far obtained and hence enhanced performance in these Van der Waal-gap engineered electrodes compared to GO. These modified materials are also compatible with Li-battery recycling technology³².

2. Materials and Methods



2.1 Synthesis of Intercalated Li-GO-EnBoc nanosheets

View Article Online
DOI: 10.1039/D4YA00217B

2.1.1 Synthesis of Mono-Boc Ethylenediamine (EnBoc)

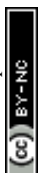
The selective EnBoc was performed according to a previously described method.³³ In brief, 10 molar equivalent of ethylenediamine was placed in a 100 mL of dry chloroform in a round bottom flask and cooled to 0°C. To this mixture *tert*-butyloxycarbonyl carbonate (CAS #: 24424-99-5, Sigma Aldrich, India) in 70 mL of dry chloroform was added dropwise with constant stirring over a 3 h period. The resulting milky solution was washed with water and then extracted with diethyl ether. During rotary evaporation of the solvent, the unreacted amine was removed and stored under high vacuum to remove the residual solvent. The desired product was isolated as a gummy thick liquid. (Yield- 82%).

2.1.2 Intercalation of EnBoc on the GO nanosheets: GO-EnBoc

The GO nanosheets were prepared as described elsewhere.³⁴ Briefly, EnBoc in tetrahydrofuran (80 mL) was added dropwise for 6 h with constant stirring at 5-8 °C into the dispersed GO sheets (1 gm) in 100 mL of double distilled water. The stirring was continued at room temperature for 3 days. A clear colour change from brown to black was observed. The residue was washed with ethanol, acetone and diethyl ether to isolate it as a free-flowing black solid (850 mg).

2.1.3 Preparation of Li-GO-EnBoc nanosheets

Lithium-ion intercalation was performed by dispersing GO-EnBoc nanosheets in 100 ml ethylene carbonate (CAS #: 96-49-1, Sigma Aldrich, India) followed by ultrasonication for 30 m and then cooling to 0 °C. LiClO₄ (1 g) in 70 mL of ethylene carbonate was added to this solution over a period of 3 h. The reaction mixture was stirred at room temperature for 36 h and the resulting black solid was centrifuged and washed with methanol, acetone, and diethyl ether and stored (Yield: 650 mg, 68%) (Figure 1).



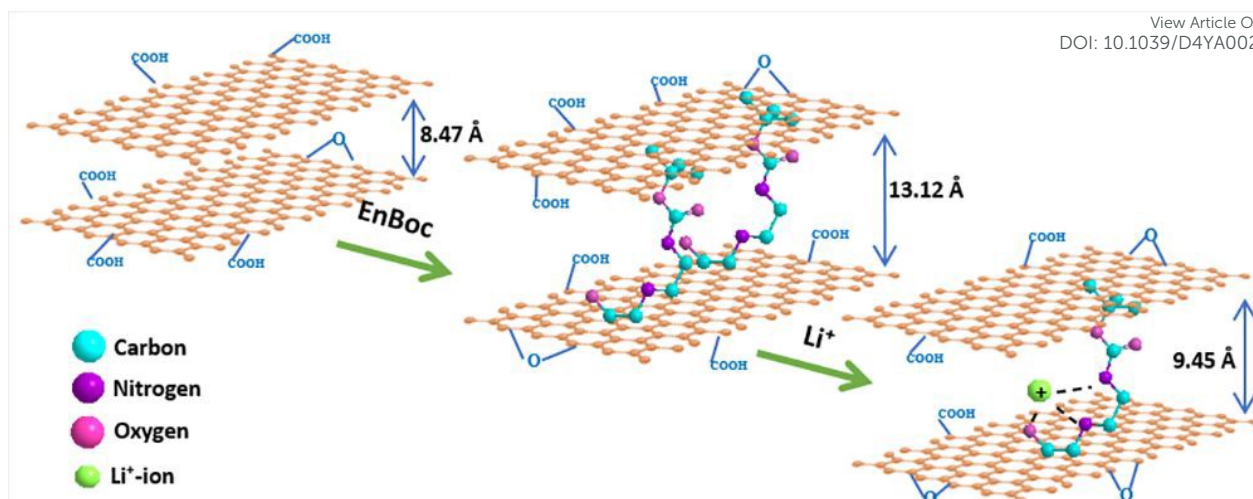


Figure 1. Schematic illustration (not to scale) of the synthetic methodology to indicate the change in length scales after anchoring of EnBoc in between the GO basal planes and subsequent intercalation of Li^+ ions.

2.2 Material Characterisation:

Raman spectra were obtained using a custom-built NIR Raman microscope with inverted geometry by placing samples on top of quartz coverslips with a 15 mW, 785 nm excitation laser and integrating the generated signal for 2 m. SEM images were taken using a Carl Zeiss Supra 25 FESEM. FTIR analysis for the GO-based active material was carried out in a spectral range of 450 to 4000 cm^{-1} using the Perkin-Elmer ATR C117460 instrument. Powder X-ray Diffraction of the samples was recorded on a Smart Lab 9 Kw -Rigaku with a monochromatic $\text{Cu K}\alpha$ source ($\lambda = 1.5406 \text{ \AA}$) at 45 kV and 200 mA. X-ray photoemission spectroscopy (XPS) measurements were performed on an XPS instrument (Carl Zeiss) using ultra-high vacuum with $\text{Al K}\alpha$ excitation at 250W. High-Resolution Transmission Electron Microscope (HRTEM) JEOL JEM 2100 was used to observe a lattice resolution of 0.14 nm and point-to-point resolution of 0.19 nm with 200 kV acceleration voltage and Gatan Orius 2K x 2K CCD camera for image recording/processing. Atomic force microscopy (AFM) analysis was performed using a Cypher AFM instrument (Asylum Research, Santa Barbara, CA) and a standard AC-160 tapping mode tip to image topography of graphene oxide (GO) material. The graphene



oxide sheets were prepared by applying the GO powder onto blue tape and transferring it to a Si/SiO₂ substrate using the exfoliation method. The height images were masked and flattened using instrument software. Solid-state NMR spectra were recorded with a 500 MHz Bruker Advance III HD wide-bore spectrometer. For ¹³C-NMR, the samples were loaded into a 3.2 mm rotor closed with a vessel cap, and measured with a triple-tuned HCN MAS probe under magic angle spinning (MAS) of 20 kHz. The signal was acquired for 40 ms under 50 kHz ¹H decoupling, after an initial 30° pulse of 1.33 μs. Approximately 10000 scans separated by a recycle delay of 5 s was accumulated. ⁶Li and ⁷Li NMR spectra were performed on samples filled into a 2.5 mm rotor, which was spun at 25 kHz in a double-tuned HX MAS probe. ⁶Li NMR spectra were acquired for 65 ms after a 1 μs pulse, accumulating 200000 scans separated by 3 s recycle delay. ⁷Li NMR spectra were acquired for 80 ms after a 2 μs pulse, accumulating 10000 scans separated by a recycle delay of 0.3 s. A rotational echo double resonance (REDOR) experiment was performed to measure ⁷Li to ¹H proximities. For this experiment, a series of ⁷Li NMR spectra was acquired using the above 2.5 mm HX MAS probe, where the acquisition was preceded by a sequence of rotor synchronized 180° pulses of 6.4 μs on the ¹H channel to cause recoupling of the ⁷Li-¹H dipolar coupling. The pulses were separated by half rotation periods, and the central pulse was replaced by a 180° pulse on the ⁷Li channel. The length of the recoupling period was varied to obtain a REDOR curve. This curve was compared to theoretical curves, calculated using self-written software, to obtain a distance estimate.

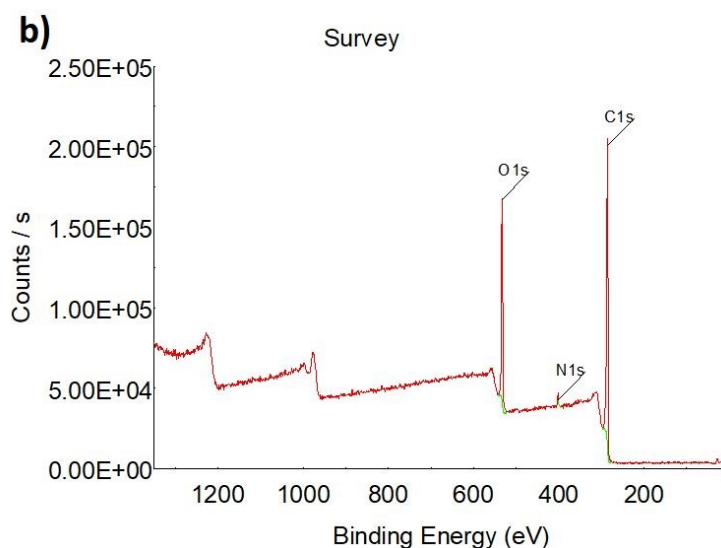
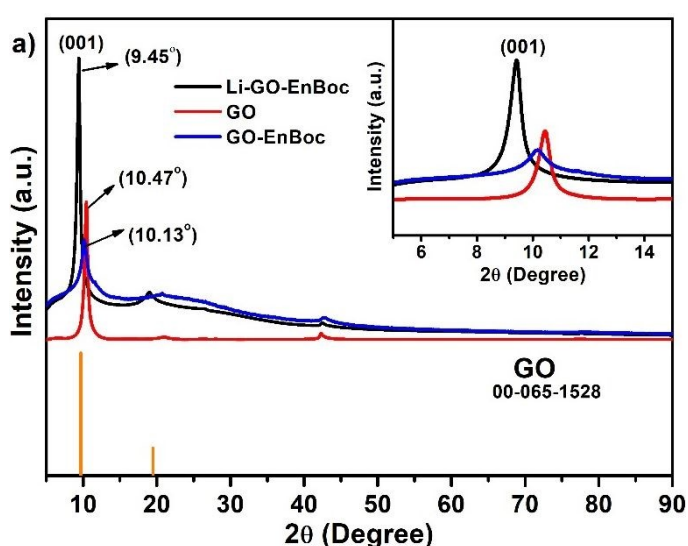
2.3 Electrochemical measurements-

A composite electrode was fabricated from 50 % of Li-GO-En-Boc, 20 % conductive additive (acetylene black), and 30 % binder (teflonized acetylene black, TAB-2) with ethanol using a mortar and pestle (Figure S1). The GO-EnBoc electrode was also prepared in the same manner as Li-GO-EnBoc. A thin film (2.7 μm) of the electrode was pressed onto a 200 mm² stainless steel mesh (Goodfellow, UK), which acted as a current collector. The GO electrode



was fabricated by slurry coating method using a doctor blade. In a typical procedure, 90 % GO was mixed with 10 % binder (polyvinylidene fluoride) to obtain a homogenous slurry by stirring overnight. Subsequently it was coated on a pre-treated Cu-foil with a doctor blade, and the coated foil was dried in a hot air oven and then pressed under a hot roll press (Tester Sangyo, Japan). Disc electrodes of 12 mm diameter were punched out with the help of an electrode cutter. The active material loading in Li-GO-EnBoc is 3.25 mg cm^{-2} while for GO is $\sim 1.32 \text{ mg cm}^{-2}$. The as-prepared electrodes were dried in a vacuum oven at 75°C overnight, prior to cell assembly in an Ar-filled glovebox. The CR2016 cells were made with glass microfiber separators (Whatman, cat no. 1825-047, UK) using 1 M LiPF_6 in ethylene carbonate (EC): dimethyl carbonate (DMC) (1:1 v/v) as electrolyte (Tomiyaama, Japan). Battery tester BCS 805 (Biologic, France) was used for galvanostatic charge/discharge and cyclic voltametric studies of Li-GO-En-Boc, GO-EnBoc and GO electrodes. Electrochemical Impedance studies were performed for the electrodes at open circuit voltage using an AC amplitude of 5 mV (RMS value) in the range of 1 MHz-0.1 Hz using Solartron 1470E electrochemical workstation.

3. Result and Discussions



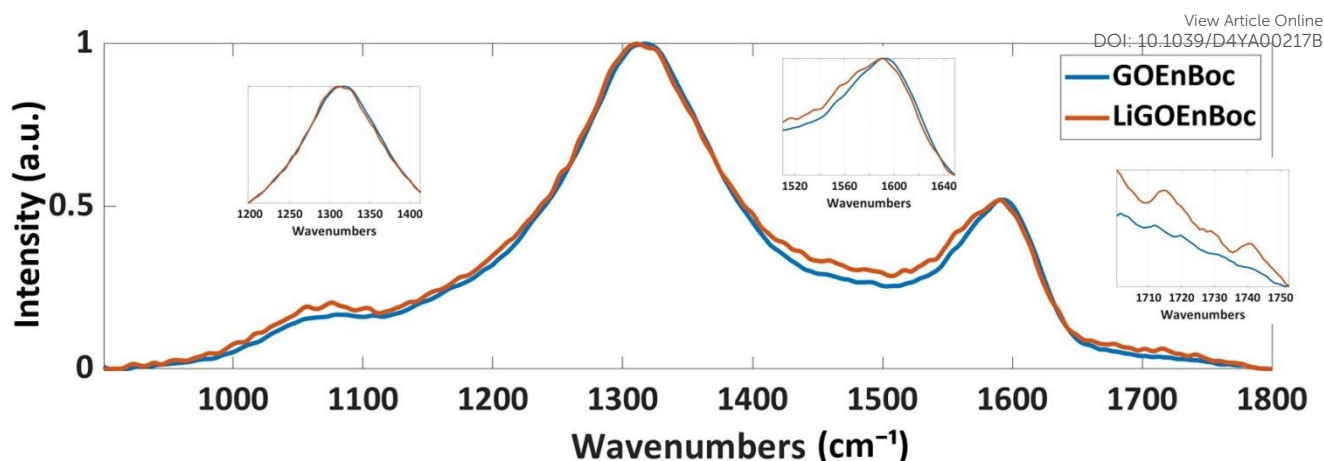


Figure 2: A Comparison of the (a) Powder X-ray Diffraction (XRD) profile of GO, GO-EnBoc, and Li-GO-EnBoc, (b) XPS survey profile of GO-EnBoc and (c) Raman Spectra of GO-EnBoc and Li-GO-EnBoc.

The quality and the degree of functionalization of GO nanosheets are determined by X-ray diffraction (XRD), Fourier transform infrared spectroscopy (FT-IR), X-ray Photoelectron spectroscopy (XPS), Raman Spectroscopy and Solid-state ^{13}C -MAS-Nuclear Magnetic Resonance (SS-NMR). The difference in the inter-layer spacing of GO nanosheets with the covalent anchoring of GO-EnBoc with and without Li-ions was confirmed by XRD analysis. The chemical functionalization with heteroatoms on the basal planes of GO nanosheets often results in the formation of reduced oxygen content in the basal planes, referred as Reduced Graphene oxide (*rGO*), with a corresponding peak at $2\theta \sim 26^\circ$. Accordingly, figure 2(a) and S2 reveal a sharp peak (001) with an enhanced *d*-spacing from 8.71 Å to 13.17 Å for GO and GO-EnBoc respectively, as a result of the intercalation of mono Boc protected amines on the GO basal plane. More interestingly, this *d*-spacing due to the chemical functionalization of GO basal plane decreases (9.35 Å) after the Li-ions insertion (Figure 2a). The decrease in intensity for GO-EnBoc perhaps arises due to the variation in the crystallite size and the conformational change of EnBoc molecule on the GO basal plane; arises because of multiple types of adsorbed



lithium due to different relaxation time or the low amounts of anchored molecules, as discussed in the NMR section and Figure S2

In addition, detailed structural changes and surface properties are elucidated by FT-IR, XPS and Raman analysis. The modifications of the functional group upon intercalation are analysed by FT-IR (Figure S3). The formation of amino alcohol moieties is confirmed by the presence of a broad peak $\sim 3300\text{ cm}^{-1}$. The peak $\sim 1620\text{ cm}^{-1}$ corresponds to the stretching vibrations of C=O groups. Li-GO-EnBoc shows various IR peaks due to the insertion of lithium ions on the basal planes and with the coordination moieties. The predominant functional groups on the graphene nanosheets such as C-N, C-O stretching, C-H bending, appear at 1240, 1155, 1045 cm^{-1} and 1464 cm^{-1} , respectively, for Li-GO-EnBoc and GO-EnBoc.

The chemical nature and the binding energies of the elements present on the surface of GO-EnBoc are investigated by XPS analysis (Figure 2b). For example, a typical survey spectrum of GO-EnBoc shows a significant peak at 399.8 eV corresponding to the N1s binding energy confirming the covalent functionalization on the GO surface. The de-convolution of C1s and N1s in the high-resolution shows different carbon and nitrogen components are present in the functionalized GO surface. C1s XP spectra of GO-EnBoc (Figure S4 a) can be deconvoluted into three components. The peaks centred at 284.4 eV are typically attributed to the C-C bond of the graphitic network, while the peak at 286.5 eV is from the C-N bond. The highest binding energy peak at 287 eV is assigned to the presence of C=O in the terminal carboxyl groups. N1s XP spectral peak (Figure S4 b) can be deconvoluted into two components at 399.8 and 401.3 eV attributed to amine and imide groups respectively.³⁵ The atomic fractions of GO-EnBoc element are C - 73.78 %, N - 4.79 % and O - 21.42 %. Structural changes relevant to surface defects, occurring during the covalent grafting process from pristine GO to GO-EnBoc and to Li-GO-EnBoc can be analysed by Raman spectroscopy, Figure 2(c). Interestingly, the spectra display the two characteristic peaks, G band ($\sim 1590\text{ cm}^{-1}$) and D band ($\sim 1325\text{ cm}^{-1}$) which



correspond to the first-order scattering of the E_{2g} mode and the disordered structures, respectively.³⁶ The G and D band have broadened and there is also an increase in the D/G ratio ($I_D/I_G \sim 2$), suggesting that extensive oxidation has induced a significant reduction in the average size of the in-plane sp^2 domains.³⁷ There is an additional broad peak at $\sim 1050\text{ cm}^{-1}$, attributed as D^* band for both GO-EnBoc and Li-GO-EnBoc that reveals the oxygen content in the GO nanosheets.³⁸ Two additional peaks at ~ 1715 and 1742 cm^{-1} , for Li-GO-EnBoc can be seen, indicating the intercalation of Li^+ ions in the GO nanosheets.³⁹

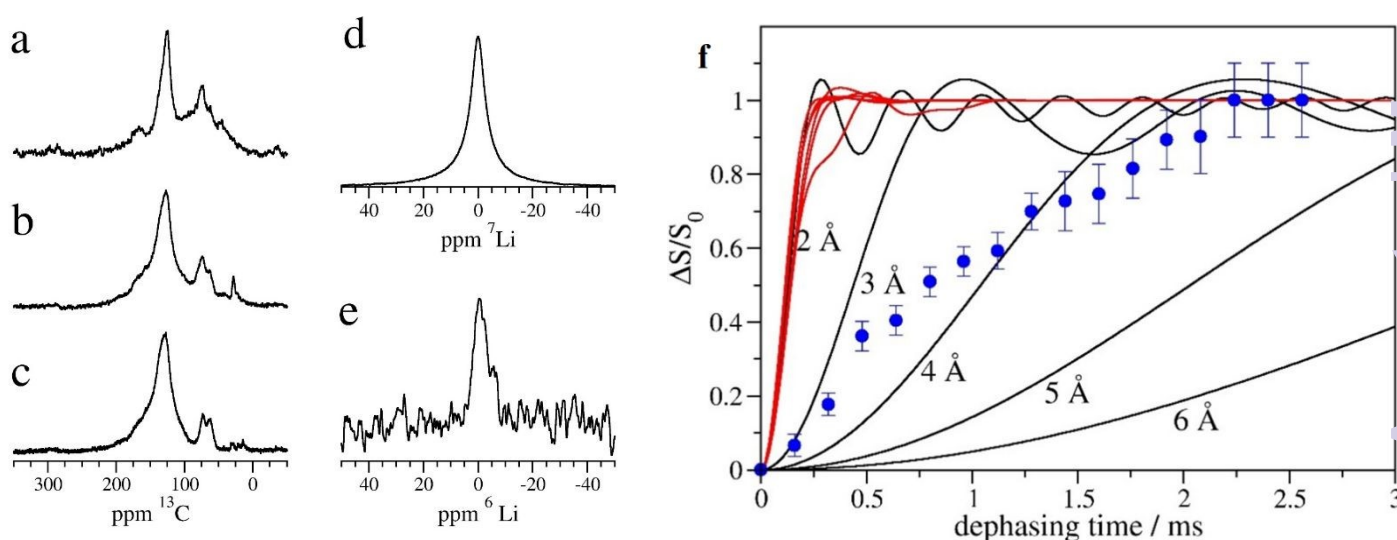
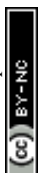


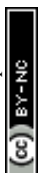
Figure 3: NMR: ^{13}C (a-c), ^7Li (d) ^6Li and (e) Li-GO-EnBoc. For comparison, the ^{13}C NMR spectra are shown also for the precursors GO-EnBoc (b) and GO (c). The ^7Li and ^6Li NMR spectra were acquired with MAS of 25 kHz, the ^{13}C NMR spectra were acquired with 20 kHz MAS. Short 30° pulses were used for initializing to reduce the effects of saturation. Recycle delays were 0.3 s, 8 s and 5 s in the case of ^7Li , ^6Li and ^{13}C NMR, respectively. f) REDOR experiments were performed to elucidate the proximity of Li and hydrogen. ^7Li NMR spectra under 25 kHz MAS were acquired after different dephasing periods, during which the ^7Li - ^1H dipolar coupling was reintroduced by RF pulses. The decay curves (blue) are indicative of the distance between the Li atoms and surrounding hydrogens. Different curves have been calculated for ^7Li - ^1H spin pairs with inter-nuclear distances of 2-6 Å as indicated (black solid lines), to allow an estimate of the Li-hydrogen distance. Theoretical curves have also been calculated for the Li ion and hydrogen coordinates of the DFT models (red solid lines).

To characterize the Li-inserted GO-EnBoc sample, we performed solid-state NMR experiments under magic angle spinning of 20-25 kHz spinning speed. ^{13}C NMR spectra were



acquired for Li-GO-EnBoc (Figure 3a), as well as for the precursor materials GO-EnBoc (Figure 3b) and GO (Figure 3c). The three materials show similar signals and differ mainly in the intensity of the individual peaks. The dominant signal at 125 ppm can be assigned to the graphene network.⁴⁰ The second largest signal in the Li-GO-EnBoc spectrum (Figure 3a) at 73 ppm, is possibly due to hydroxide modifications in graphene oxide. Similarly, the signal at 62 ppm may represent oxygenated carbon sites such as C-O-C epoxy moieties. In addition, small signals appear at ~45 ppm and ~165 ppm, which can be assigned to aliphatic, quaternary or tertiary carbon atoms and carbonyl moieties, respectively. Comparing the Li-GO-EnBoc spectrum (Figure 3a) with the GO-EnBoc and GO precursor samples (Figure 3b, c), the spectra agree well in the main signals at 125 ppm and at 73 ppm respectively. However, the GO-EnBoc sample (Figure 3b) exhibits a stronger signal at 62 ppm, which is even larger in the spectrum of GO (Figure 3c). On the other hand, both GO-EnBoc and GO nearly lack the carbonyl signal at 165 ppm, indicating that during the processing of GO epoxy-like oxygenated species might be oxidized to carbonyl. A further notable difference is a signal at 28 ppm in the spectrum of GO-EnBoc (Figure 3b), which is much lower in the spectrum of GO (Figure 3c), and absent in the Li-GO-EnBoc sample (Figure 3a). This signal may be attributed to the *t*-butyl moieties of the Boc protection group, which are cleaved of and removed during the acid washing process. It is therefore conceivable that the diamine reacted with the graphene oxide structures during processing and was incorporated covalently into the graphene oxide structure. Some minor signals in the range of 10-30 ppm, which are observed in the GO but not in the Li-GO-EnBoc sample, could be small aliphatic modifications in the graphene oxide, which are removed during processing.

The ⁷Li and ⁶Li NMR spectra (Figure 3, d, e), of Li-GO-EnBoc show a single, relatively sharp signal near 0 ppm. In addition, a second small signal can be seen at ~ -5 ppm in the ⁶Li NMR spectrum. This second minor component is absent from the ⁷Li NMR spectrum, possibly due



to a faster T_2 relaxation caused by a larger quadrupole moment in the case of ^7Li . The ^7Li chemical shift has been correlated to the staging number of the graphene sheets and the Li concentration in intercalated Li graphite compounds.⁴¹⁻⁴³ A ^7Li chemical shift of around 0 ppm, as observed in this study for the major fraction of lithium, has been ascribed to staging numbers of larger than 3-4, and to LiC_n compounds with $n \geq 36$. Lower chemical shift values, as observed in the ^6Li NMR spectrum for a minor fraction of the sample, have been assigned previously to the solid electrolyte interface layer,⁴² and may indicate a small proportion of Li ions outside of graphene-layered structures.

To elucidate the neighbourhood of the Li atoms in the Li graphene oxide samples, we measured the dipolar couplings between ^7Li and ^1H using the REDOR (rotational echo double resonance)⁴⁴ experiment (Figure 3f). In this experiment, the averaging effect of the magic angle spinning is partially compensated by a train of radiofrequency pulses effecting one type of nuclei (^1H in our case). In this way, the dipolar couplings involving the irradiated nucleus are reintroduced for a certain period (dephasing time), and lead to a reduction of the measured spectrum of an observed nucleus (^7Li in our case). The signal reduction has been measured for a number of dephasing times, and is shown in (Figure 3f). A significant reduction in signal is observed, indicating that ^7Li is close to ^1H . When comparing the experimental curve with curves calculated for ^7Li - ^1H pairs at specific distances (black solid lines in Figure 3f), the distance of Li to nearby hydrogen atoms would be around 4 Å. As most hydrogen is associated with the graphene oxide layers or with the chemical modifications, we can conclude that the Li atoms are integrated into the graphene oxide structure, or near the diamine moieties. In addition, we calculated the REDOR curves which would result from the structures obtained in the DFT simulation (red solid lines in Figure 3f). The curves look quite similar for all 6 Li ion positions evaluated in the DFT calculations. The experimental results (blue symbols in Figure 3f) do not agree with the simulated results for the DFT models but would correspond to longer



Li-hydrogen distances than in the DFT models. A possible explanation could be that Li^+ occurs in different environments with some Li^+ ions in sites near the diamine modifications, as determined by the DFT calculations, and some at sites further away from hydrogens, e.g., near graphene oxide layers. Such heterogeneity would be compatible with the ^6Li spectrum (Figure 3e), where also 2 signals are also observed.

Morphological and Structural Characterization:

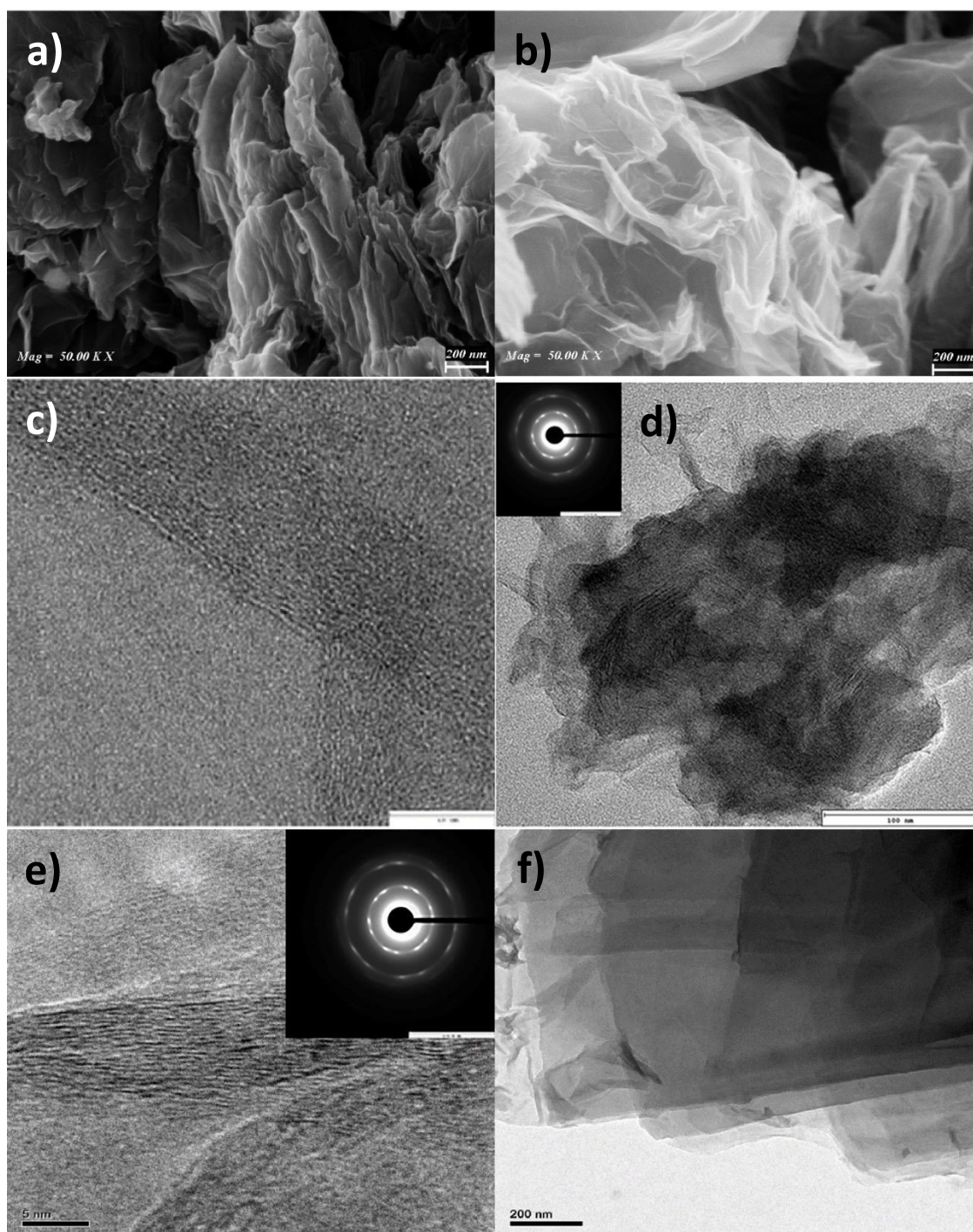


Figure 4: Field Emission-Scanning Electron Microscopic (FE-SEM) images of (a) GO (b) Li-GO-EnBoc; High Resolution-Transmission Electron Microscopic (HR-TEM) images of (c, d) Li-GO-EnBoc and (e, f) GO-EnBoc nanosheets (Inset: SAED Image)

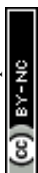
HR-TEM and FE-SEM are used for structural characterization for the GO, GO-EnBoc and Li-GO-EnBoc. During the covalent conjugation through the ring opening of epoxide the En-Boc molecules are incorporated between the layers of graphene by the nucleophilic attack of the primary amine. This covalent conjugation between En-Boc and GO results in a wrinkled sheet like morphology, and this stacked architecture of the Li-GO-EnBoc composite can be clearly observed in the scanning electron microscopy (SEM) image, Figure 4(a and b) GO and Li-GO-EnBoc. For, Li-GO-EnBoc, these sheets are much thinner suggesting after covalent grafting with EnBoc, the *d*-spacing of GO nanosheets has increased with higher surface area and interwoven porous 3D network, without disrupting the morphology of GO, which indirectly supports the XRD patterns. By contrast, SEM images of bare GO (Figure 4a) exhibit a cross-linked porous 3D network with graphene flakes interwoven throughout the structure.⁴⁵ The EDX mapping images for GO-EnBoc and Li-GO-EnBoc are shown in figure S5, which reveal that oxygen and nitrogen are evenly distributed in the GO nanosheets. Also, from Tables S1 and S2, we observed a significant change in the ratio of atomic weight percentage of carbon to nitrogen, from GO-EnBoc (C:N ~ 13:1) to Li-GO-EnBoc (C:N ~ 27:1) and a slight change in carbon to oxygen ratio from GO-EnBoc (C:O ~ 4.8:1) to Li-GO-EnBoc (C:O ~ 5:1), suggesting that the Li-ions are in multiple sites with the functionalised N- and O-atoms of the EnBoc molecule as bolstered by DFT and solid-state NMR results. Figure 4(f) shows HR-TEM image of the GO-EnBoc revealing few layers of intercalated GO nanosheets with a sheet-like rippled and crumpled layered morphology which enhanced the interlayer-spacing from 8.47 Å to 13.12 Å whereas, drastic wrinkling is visible in the Li-GO-EnBoc (Figure 4d)



nanosheets due to the insertion of Li^+ ions, which interacts with the heteroatoms (N, O) of EnBoc with an interlayer-spacing 9.45 Å from 13.12 Å. The similarity of the GO-EnBoc and Li-GO-EnBoc sheet structure suggests that the insertion of Li^+ ions occur without disrupting the layered morphology of nanosheets. Furthermore, Figure 4(c and e) shows important changes in the stacking sheet structure of GO-EnBoc and Li-GO-EnBoc as evident in the TEM cross-sections where the layers of the GO nanosheets can be discerned clearly. According to these figures, the sheets are parallelly stacked with no major ordering and covalent grafting appears to be uniform. The insets of Fig.4(d and e) show the selected area electron diffraction (SAED) patterns suggesting crystallinity, with no preferred stacking order with the covalent grafting of En-Boc within the GO nanosheets.⁴⁶ Figure S6(a) shows typical AFM image to give a rough idea on the thickness of the individual sheets. The height profile, Figure S5(b and c) of Li-GO-EnBoc indicates average thickness varying between 2-20 nm, which corresponds to about 7-20 layers either due to the stacking of functionalised GO nanosheets by or the presence of functional groups containing oxygen in the GO created by the oxidation process or by the anchoring of the EnBoc molecule in the GO basal planes.^{47,48}

Density Functional Theory (DFT) Studies:

The first principles DFT⁴⁹ calculations were performed using the Vienna *Ab Initio* Simulation (VASP) package^{50,51} with the projector-augmented wave (PAW) potentials,^{52,53} where Li 1s2s, Na 2p3s, C 2s2p, O 2s2p, N 2s2p, H 1s electrons are treated as valence electrons. Perdew-Burke-Ernzerhof (PBE) exchange-correlation functional⁵⁴ based on generalized gradient approximation (GGA) was chosen for general geometry relaxation. The spin-polarized DFT-D3⁵⁵ method was adopted for an improved description of Van der Waals interaction between layers of GO structures. The wave functions of valence electrons were described using the plane wave basis set with kinetic energy cut-off 500.0 eV. The reciprocal space of graphene and graphene oxide models were meshed $18 \times 18 \times 1$ and $4 \times 4 \times 1$, respectively, using Monkhorst-Pack method.⁵⁶ The energy convergence



criterion for electronic iterations is set to be 10^{-5} eV and the force is converged to be less than 0.01 eV/Å for geometry optimization of the simulation cell.

A graphene model containing 60 carbon atoms with a cell dimension $12.34 \text{ \AA} \times 12.83 \text{ \AA}$ was selected to build defective GO model. The 2D GO model includes one carbon vacancy, 8 OH group and 3 epoxides with the chemical composition $C_{59}(OH)_8O_3$, which corresponds 1.67% vacancy density and 20 wt% of oxygen content. The bilayer GO model was created using AB stacking of the fully relaxed single layer GO structure. Intercalant molecule EnBoc was then inserted in between the bilayer GO model. The z-vector of the simulation cells was set to be 30 \AA to ensure sufficient vacuum space ($>14 \text{ \AA}$) included in the calculations to minimize the interaction between the system and its replicas resulted from periodic boundary conditions. After geometry relaxation, the interlayer distance D for the EnBoc intercalant was found to be 13.19 \AA (see figure 5), which is in excellent agreement with the experimental result of 13.17 \AA .

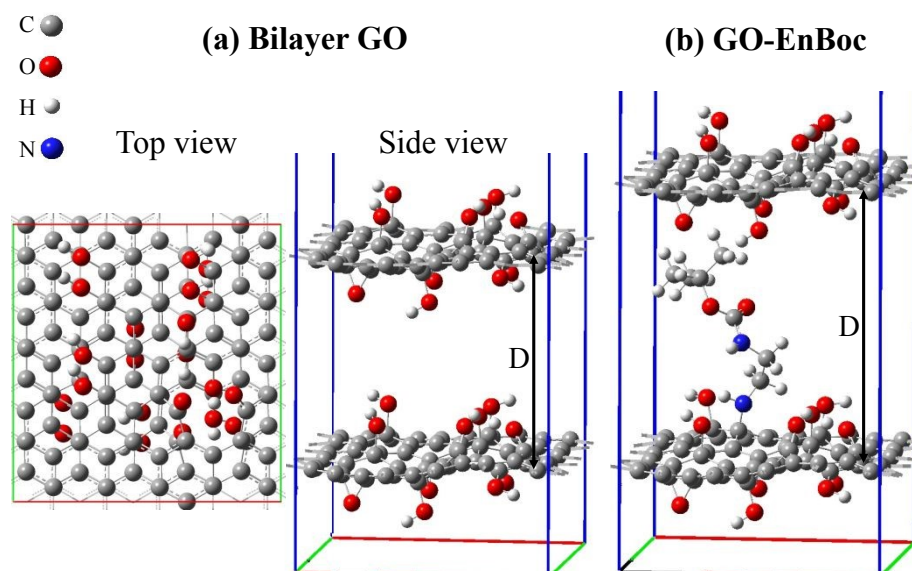


Figure 5: Snapshots of (a) the bilayer GO model in top and side views, (b) the bilayer GO with intercalant molecule EnBoc (GO-EnBoc). The red, green and blue cell edges represent x, y and z axes, respectively. The grey, red, white and blue balls denote the C,



O, H and N atoms, respectively. The interlayer distance of the bilayer GO is labelled as

View Article Online
DOI: 10.1039/D4TA00217B

D.

To study the effect of lithiation of the intercalated bilayer GO model, Li atom is added to 6 different chemical sites in the simulation cell. The binding energy and the interlayer distance D for the geometry relaxed Li-GO-EnBoc systems are calculated and reported in Table 1. The binding energy is calculated using Eq. (1),

$$B.E. = E_{\text{system}} - (E_{\text{GO-EnBoc}} + E_{\text{Li}}) \quad (1)$$

where E_{system} is the energy of the lithiated and interacted Li-GO-EnBoc system, $E_{\text{GO-EnBoc}}$ is the energy of the EnBoc molecule-intercalated GO structure, and E_{Li} is the energy per atom in bulk Li metal. The snapshots of some geometry relaxed Li-GO-EnBoc systems are presented in Figure 6.

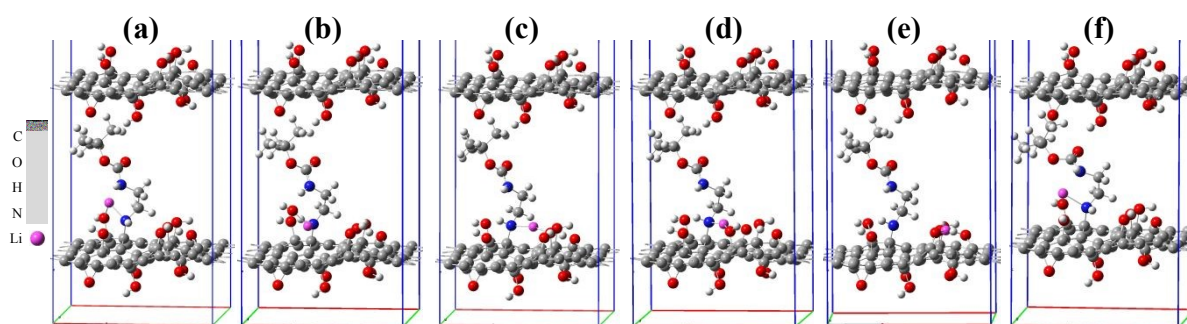
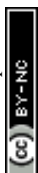


Figure 6: Snapshots of geometry relaxed Li-GO-EnBoc systems with one Li atom at the sites #1-6 (a)-(f), respectively. The red, green and blue cell edges represent x, y and z axes, respectively. The gray, red, white, blue and purple balls represent the C, O, H, N and Li atoms, respectively.

The average equilibrium lithium potentials are calculated following references^{57,58},

$$V(x) = - \frac{\mu_{\text{Li}}^{\text{cathode}}(x) - \mu_{\text{Li}}^{\text{anode}}}{zF}, \quad (2)$$

$$\Delta G_r = B.E., \quad (3)$$



$$V(x) = -\frac{\Delta G_r}{x},$$

View Article Online
DOI: 10.1039/C4YA00217B

It reflects the difference in chemical potential between the anode and cathode. F is Faraday's constant and z is the charge in electrons transported by lithium in the electrolyte. For a half-cell configuration with a Li metal anode and intercalated cathode, $V(x) > 0$ represents the discharge process. The Gibbs free energy change ΔG_r can be obtained from the binding energy and the average lithium potential is readily calculated and the results are reported in Table 1.

Table 1- The calculated binding energy, interlayer distance and average lithium potential of the geometry-relaxed Li-GO-EnBoc systems with Li insertion at six different sites. The case of six Li atom insertion into GO-EnBoc system is also listed.

System	Binding energy (eV)	Final layer distance D (Å)	Average lithium potential V (V)
Li-GO-EnBoc, Li site 1	-2.08	13.02	2.08
Li-GO-EnBoc, Li site 2	-2.97	13.17	2.97
Li-GO-EnBoc, Li site 3	-2.25	13.24	2.25
Li-GO-EnBoc, Li site 4	-3.37	12.81	3.37
Li-GO-EnBoc, Li site 5	-2.33	13.19	2.33
Li-GO-EnBoc, Li site 6	-2.29	11.30	2.29
Li-GO-EnBoc, 6 Li atoms	-16.14	13.26	2.69

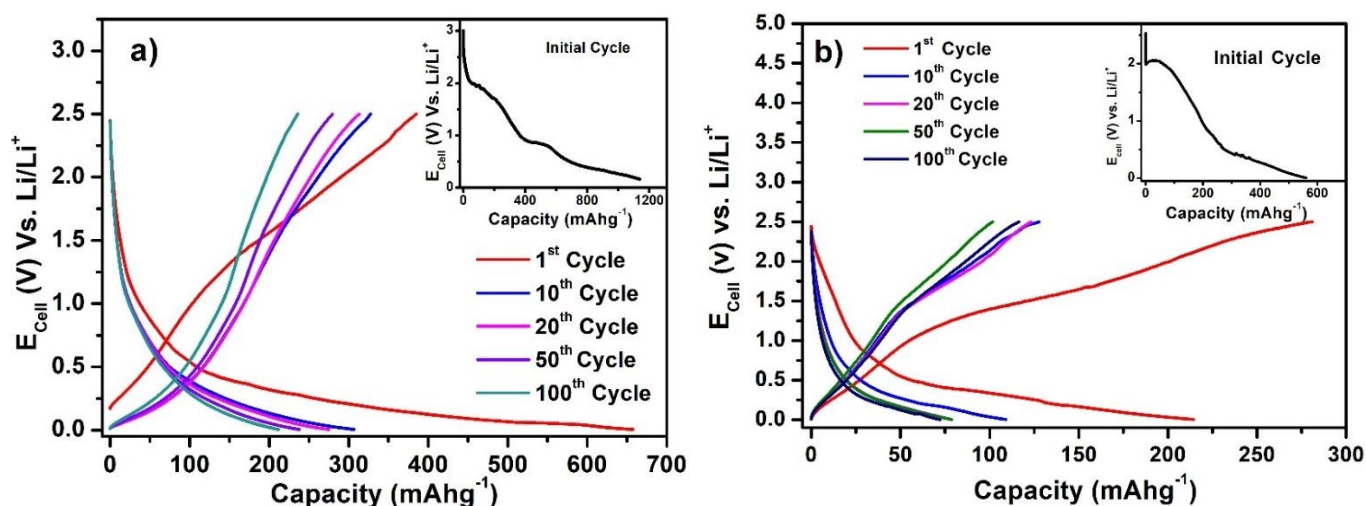
Among these six sites, the average interlayer distance D is found to be 12.79 Å and the average lithium potential is 2.55 V. The DFT calculation results are in excellent agreement with the experimental results in terms of the intercalation, thereby the enhancement of interlayer spacing. In addition, the calculated average lithium potential of 2.55 V for the Li insertion sites #1-6 agrees well with the experimentally observed cell voltage range 2.0 – 2.5 V at low capacity as presented in Fig. 7(a). The theoretical specific gravimetric capacity, C_G (in mAh/g), for our models Li-GO-EnBoc with the composition $C_{125}O_{24}H_{31}N_2Li_1$ was determined to be 13.7 mAh/g using the equation $C_G = \frac{1000xF}{3600M_w}$, where F is Faraday's constant



(9.6485×10^4 C), x is the number of Li inserted, and M_w is the molecular weight of the compound. Multiple Li insertion into the GO-EnBoc system was also considered and calculated with the composition $C_{125}O_{24}H_{31}N_2Li_6$. For the case of a total of 6 Li atoms insertion, the interlayer distance D is 13.26 Å and B.E. is -16.14 eV, which corresponds to an average lithium potential of 2.69 V at the specific gravimetric capacity of 81.0 mAh/g.

Electrochemical performance:

To evaluate the utility of these materials to reversibly store Li^+ ions and effectively allow charge-discharge performance, several electrochemical experiments are performed and the Open Circuit Voltage (OCV) is around 3.0-3.2 V for both GO and Li-GO-EnBoc showing that the system is thermodynamically viable.



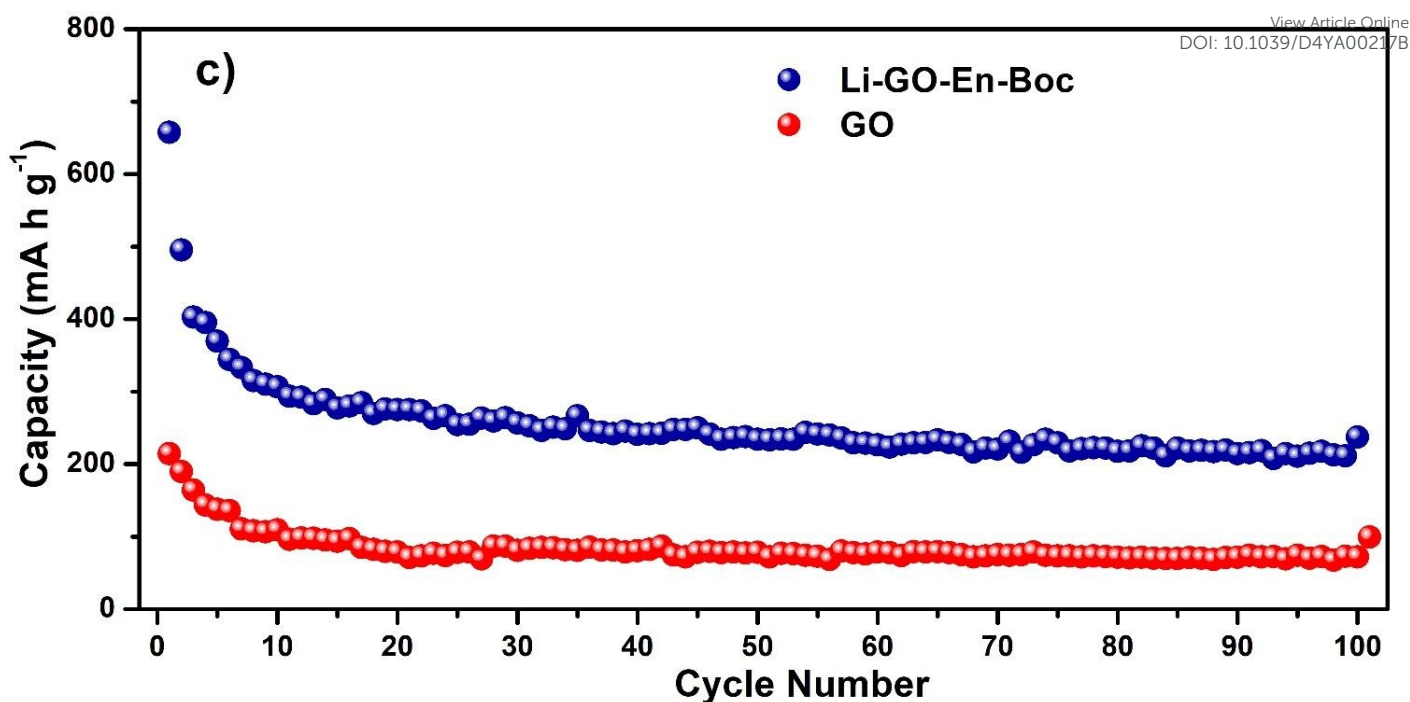


Figure 7: Charge-discharge profiles for (a) Li-GO-EnBoc and (b) GO electrode cycled at 25 mA g⁻¹ between 2.5 and 0.005 V vs Li/Li⁺ in a 1 M LiPF₆ in a 1:1 (v/v) mixture of ethylene carbonate (EC) and dimethyl carbonate (DMC) as the electrolyte. c) Variation in discharge capacity vs cycle number for GO and Li-GO-EnBoc.

Figure (7a), shows the cyclic stability of GO intercalated with (Li-GO-EnBoc), Figure (7b), GO and Figure S7, GO-EnBoc electrodes by galvanostatic charge/ discharge measurements between 0.005-2.5 V vs. Li at a rate of 25 mA g⁻¹ or 0.06 C similar to what is previously reported.⁵⁹⁻⁶¹ The Li-GO-En-Boc shows (insets) an initial discharge capacity of 1200 mA h g⁻¹, while GO shows 580 mA h g⁻¹ and GO-EnBoc shows 1280 mA h g⁻¹. The initial discharge curve (inset) shows various plateaus at around ~ 2.02, 0.9, and 0.55 V, for Li-GO-EnBoc; around 2.04 and 0.29 V for GO and around ~ 1.98, 0.97 and 0.53 V for GO-EnBoc respectively, which are attributed to the SEI (Solid Electrolyte Interphase) layer formation on the surface of the electrodes, associated with electrolyte decomposition, formation of Li-organic compounds and irreversible capacity.^{62,63} The inset of Li-GO-EnBoc and GO-EnBoc shows various plateaus to



indicate that Li-ions are intercalated at various stages, while in GO (inset) these are not very prominent, also there is a straight line of decline in the initial stage because of the conductivity change due to surface functional groups on GO during initial cycles, possibly indicating better charge acceptance. In Figure (7b), the first cycle charge capacity of GO is higher than the discharge capacity because Li-ions might get attached to the different functional groups and not all Li-ions are participating in the electrochemical reaction, while in Li-GO-EnBoc, Li-ions are mostly interacting with the amino alcohol moieties. In succeeding cycles, these plateaus disappear, and a smooth curve appears with first discharge capacity for Li-GO-EnBoc of 680 mAhg⁻¹ and a stable reversible capacity of 270 mAhg⁻¹, while GO shows first discharge capacity of 220 mAhg⁻¹ and a stable capacity of 80 mAhg⁻¹ after 100 cycles respectively. This is perhaps due to the Li⁺ insertion with a stable SEI film, Li⁺ binding and large interlayer spacing of around 13.17 Å with the covalent grafting of the organic molecules in GO as compared to pristine GO with an interlayer spacing of 8.44 Å. Figure (7c), shows the variation of Discharge Capacity with Cycling for the Li-GO-EnBoc, and GO electrodes respectively. Interestingly, these show stable reversible capacity of 270 mAhg⁻¹, and 80 mAhg⁻¹ respectively up to 100 cycles. This suggests that the covalent grafting of the organic molecules in GO has resulted in more diffusion of Li-ions and faster dynamics thus enhancing the performance.

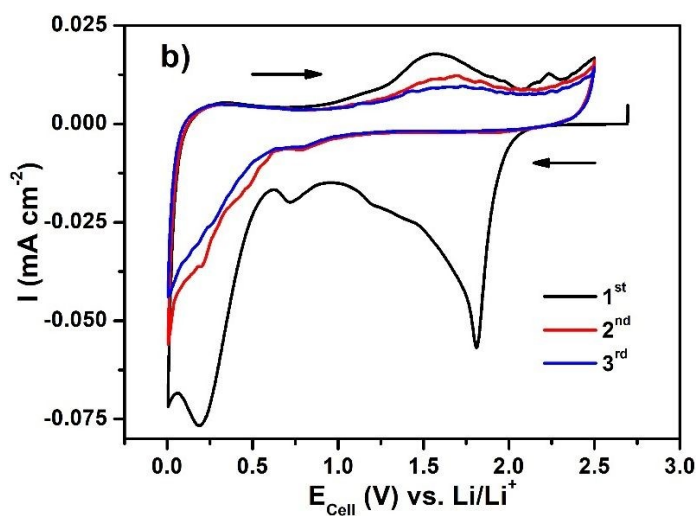
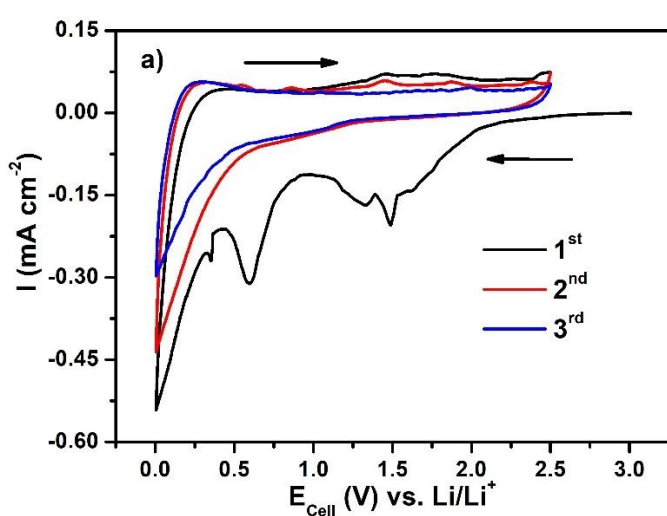


Figure 8: Cyclic voltammograms of (a) Li-GO-EnBoc and (b) GO electrode in a 1 M LiPF_6 in a 1:1 (v/v) mixture of ethylene carbonate (EC) and dimethyl carbonate (DMC) as the electrolyte with Li as counter and reference electrode at a scan rate of 0.1 mV s^{-1} .

Figure (8a), shows the Cyclic Voltammograms (CV) for Li-GO-EnBoc and Figure (8b), for GO electrodes and Figure S8 for GO-EnBoc at a scan rate of 0.1 mVs^{-1} . The CV profiles show reversible lithiation/ de-lithiation and the current profile in the first discharge differs from the rest of the cycles as the material undergoes extensive Li-ion re-organisation. This is seen in the form of a broad reduction peak at around $\sim 0.3, 0.6$ and 1.5 V vs. Li/Li^+ for Li-GO-EnBoc, $0.4, 0.6, 0.83, 1.42$ and 2.19 V for GO-EnBoc and about $\sim 0.25, 0.75$ and 1.8 V for the GO electrode. Also, during the initial cycle there is a SEI layer formation due to electrolyte decomposition at the electrode surface. In subsequent cycles, the cathodic peak is observed at $\sim 0.9 \text{ V}$ for Li-GO-EnBoc, 0.28 and 0.88 V for GO-EnBoc and $\sim 0.8, 0.5,$ and 0.25 V for GO electrodes and anodic peaks at ~ 0.26 and 1.6 V for Li-GO-EnBoc, 0.25 and 1.55 V for GO-EnBoc and observed ~ 0.35 and broad peak around 1.7 V for GO are observed respectively, showing multiple Li-ion intercalation sites.

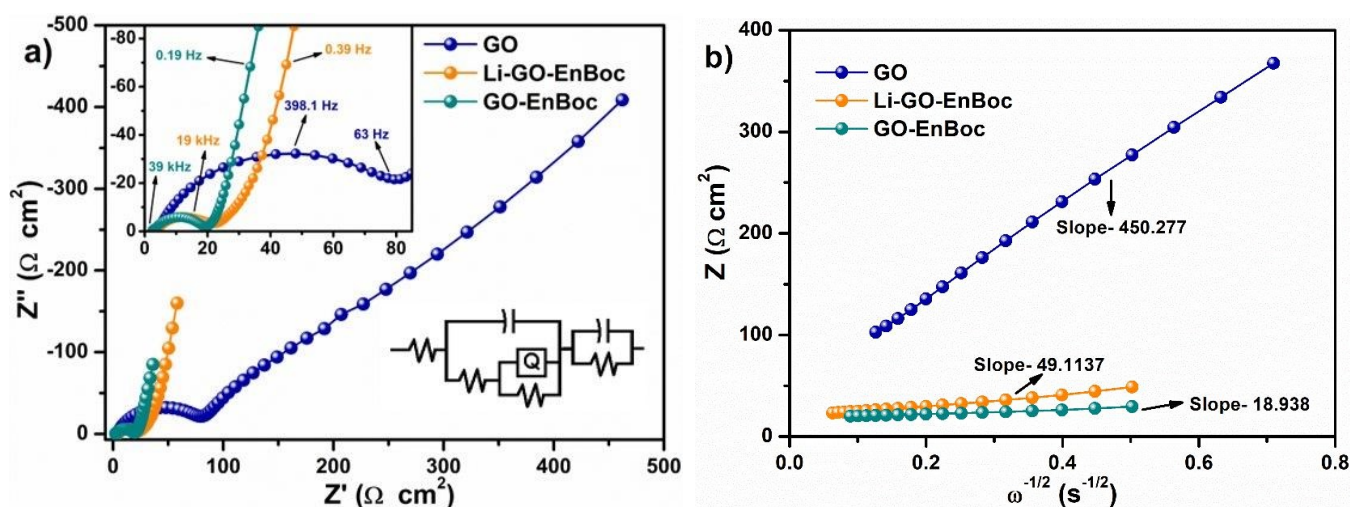


Figure 9: (a) Nyquist plots for Li-GO-EnBoc, GO-EnBoc and GO and (b) Randles plot for Li-GO-EnBoc, GO-EnBoc and GO.

View Article Online
DOI: 10.1039/D4TA00217B

Figure (9a) shows the Nyquist plot of Li-GO-EnBoc, GO-EnBoc and GO-Li. The impedance measurement is performed by initially applying a high-frequency current and then progressing toward lower frequencies. The responses observed in the high-frequency regime (semi-circle) correspond to charge transfer processes with the lower x-axis intercept value giving the solution resistance (R_s), and the higher x-axis intercepts giving the sum of solution resistance and the charge transfer resistance (R_{ct}), whereas the responses in the low-frequency regime (tail or nearly linear region) correspond to diffusion-controlled processes.^{64,65} Accordingly, Figure (9b) shows Randles plot for Li-GO-En-Boc and GO electrodes which is composed of Z' versus $\omega^{-1/2}$, whose slope is equal to Warburg coefficient (σ) in $\Omega \text{ s}^{-1/2}$. The Warburg coefficient and R_{ct} are then used to calculate the diffusion coefficient (D) in cm^2s^{-1} and exchange current density (j_0) respectively using the following equations from the impedance data-

$$\sigma = \frac{RT}{n^2 F^2 A \sqrt{2}} \left(\frac{1}{\sqrt{DC^*}} \right) \quad (1)$$

$$j_0 = \frac{RT}{nFR_{ct}A} \quad (2)$$

Where R is the gas constant, T is the temperature in K , n is the number of electrons transferred, F is Faraday's constant, A is the area of the electrode, and C^* is the concentration of the electrode. The results are shown in Table 2.

These results obviously demonstrate that modulation of the Van der Waal gap with organic molecule has enhanced the electrochemical performance of the active material. The higher D_{Li^+} for Li-GO-EnBoc (twice that on pristine GO electrode) indicates faster kinetics of the Li^+ -ions through the electrolyte channel as these heteroatoms, increasing the rate capability of the electrode.



Table 2- Comparison of Kinetic parameters of Li-GO-EnBoc, GO-EnBoc and pristine

GO electrode.

Samples	R_s (Ω)	R_{ct} (Ω)	σ (Ω s ^{-1/2})	D_{Li^+} (cm ² s ⁻¹)	j_0 (A cm ⁻²)
GO	1.8456	95.367	450	6.88×10^{-16}	4.374×10^{-5}
Li-GO-En-Boc	2.75	17.736	50	5.78×10^{-14}	1.28×10^{-3}
GO-EnBoc	2.66	19.09	19	2.076×10^{-13}	8.74×10^{-4}

Various energy storage systems with GO/rGO functionalized anode materials having other electroactive components have been compared and Li-GO-EnBoc (without other electroactive components) displayed quiet comparable performance in terms of capacity and stability as shown in Table 3.

Table 3- A Comparison of the electrochemical performance of Li-ion Batteries (LIBs) with Carbon Anodes.

Anode Materials	Discharge Capacity (mAhg ⁻¹)	Current Density (mA g ⁻¹)	Potential Window (V)	Ref.
Graphene acid	1234	100	0.01-3	66
N-rGO film	529	100	0.01-2.5	67
rGO / FePc	441	50	0.01-3	68
Li-rGO	>1000	25	0.02-3	60
GO-THBQ	1075	50	0.01-3	69
Tp-THzT-CIN/r-GO	123	50	0.01-3	70
rGO@NDC	1400	0.5 C	0.01-3	71
P(C-TDPP-AC)/RGO	857	1000	0.01-3	72
AQGO	467	5000	0-3	73
GO	220	25	0.005-2.5	This work
Li-GO-EnBoc	680	25	0.005-2.5	This work



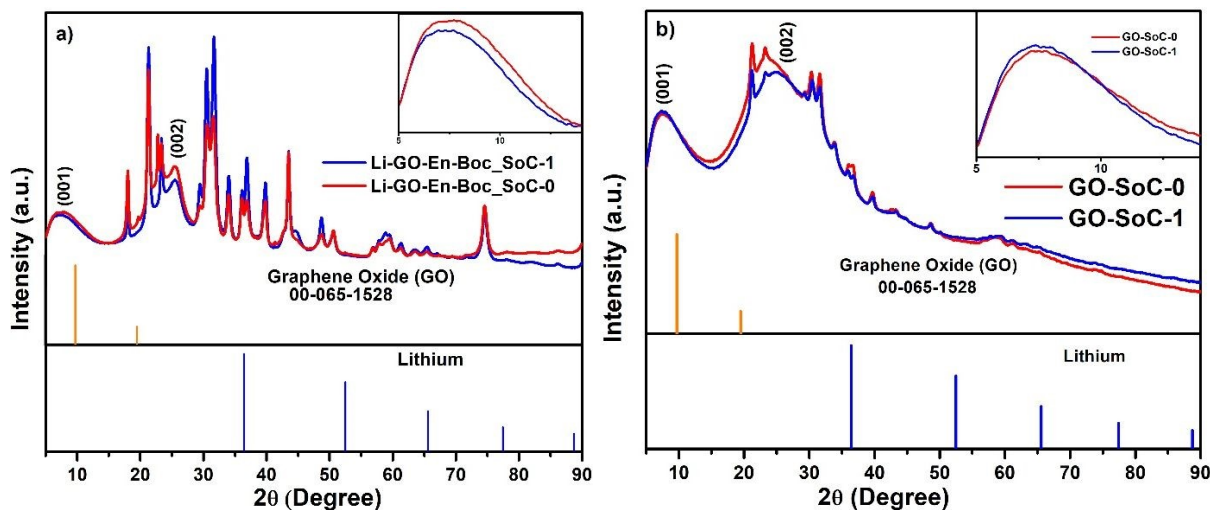
Post-mortem Analysis:

Figure 10: XRD profiles at State of Charge ~ 0 (After 1st Discharge cycle) and 1 (After 100th charge cycle) for (a) Li-GO-EnBoc and (b) GO

Figures (10 a) and (10 b) show comparative XRD profiles of the Li-GO-EnBoc and GO electrodes at States of Charge (SoC) close to 0 and 1. This is used to study the structural evolution of the material before and after a typical charge-discharge cycling. Interestingly, in both the figures, the (001) plane of GO has broadened while the (002) plane has emerged prominently for both SoC-0 and 1. In figure (10 a), the *d*-spacing of (001) plane (inset) has shifted from 14.09 Å (SoC ~0) to 14.35 Å (SoC~1) respectively, suggesting volume changes associated with Li incorporation while, in Figure (10 b), the *d*-spacing of (001) plane (inset) has changed at SoC ~0 and 1 are 13.25 Å to 13.7 Å respectively and the difference in interlayer *d*-spacing during SoC 0 and 1 is of 0.45 Å, while for Li-GO-EnBoc, it is 0.26 Å. This suggests that volume changes associated with SoC ~0 and 1 has decreased to half with specific functionalisation of GO-EnBoc depicting structure is more robust for Li-GO-EnBoc during lithiation and de-lithiation. This plays an important role in alleviating the stresses involved during cycling.



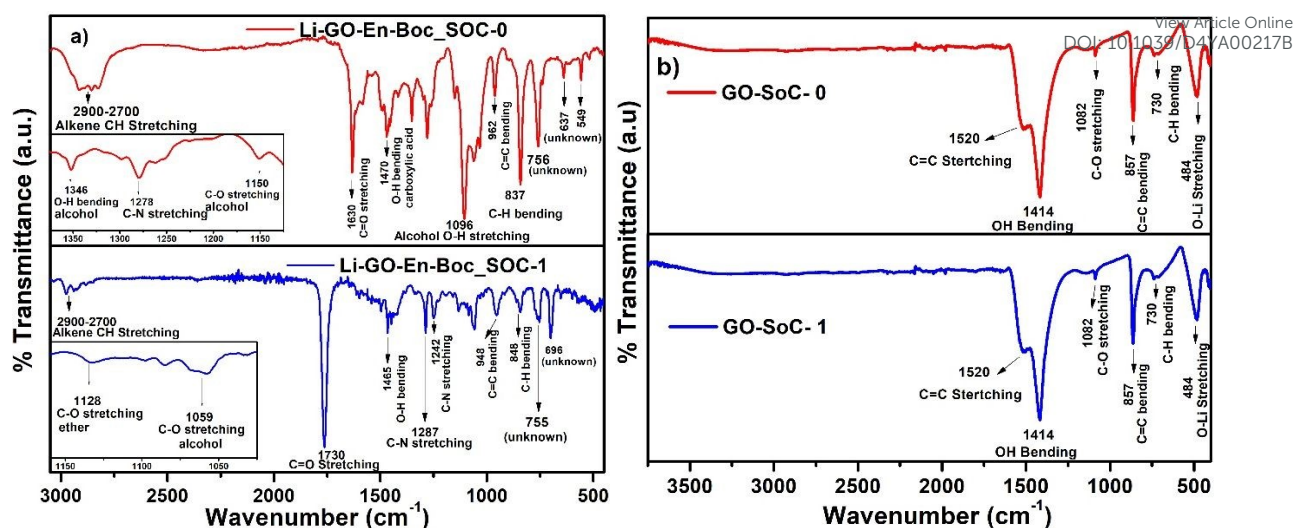


Figure 11: Comparative FT-IR of (a) Li-GO-EnBoc and (b) GO at States-of-Charge (SoC) ~ 0 (After 1st Discharge cycle) and 1 (After 100th charge cycle).

The Figure (11 a) shows that in Li-GO-EnBoc, the Li-ions are more mobile as in both SoC ~ 0 and 1, O-Li peaks are not obtained, which usually comes around 500 cm^{-1} , while Figure (11 b) shows that in GO, the Li-ions are strongly associated with the graphene network, and a sharp peak for O-Li bond is visible at 484 cm^{-1} at both SoC ~ 0 and 1 respectively.^{74,75} It is also observed that in both the materials, Li-ions interact with the same kind of environment as most peaks in FT-IR is similar. These results are in excellent agreement with the data obtained from NMR, which is an independent technique.

Conclusions:

Lithium intercalation continues to hold a pivotal role in shaping the applications of currently used Li-ion batteries (LIBs). This study demonstrates that the electrochemical performance and kinetics of the Graphene-based materials can be enhanced through the modulation of the interlayer gap via the covalent anchoring of ethylenediamine through the ring opening of epoxide by the nucleophilic attack of the primary amine. The synthesized Li-GO-EnBoc material exhibits faster Li^+ kinetics owing to a higher Li-ion content and co-ordination with the heteroatoms such as N and O of EnBoc molecule, thereby improving the electrode's rate



capability. Notably, the covalent intercalation of t-butyl moiety-bound ethylenediamine on the GO basal planes leads to an enlarged interlayer d-spacing (from 8.47 Å to 13.17 Å) without reducing it to rGO, enabling more Li ions to be reversibly accommodated with better mobility. Comprehensive characterization using ^{13}C , ^7Li , ^6Li -MAS NMR, XPS, IR, Raman, and microscopy confirms the accommodation of Li^+ ions at multiple sites. This, along with an enhanced diffusion coefficient, contributes to an improved capacity value of 270 mAhg $^{-1}$ after 100 cycles with perhaps a negligible fading. The improved electrochemical performance is further corroborated by DFT calculations and solid-state NMR measurements, laying a solid foundation for the potential application of functionalized Van der Waal gap GO-engineered materials as efficient anodes for Li-ion batteries.

Acknowledgments: The authors sincerely thank the UGC-DAE-Consortium Scientific Research, Kalpakkam Node (No. CSR/Acctts/2016-17/1347) and DST-TDT, DPRP division (No.:VI-D&P/562/2016-17/TDT(C)) for their funding to carry out the research. Dr. S.L. Grage would like to acknowledge support by the instrument grant INST 121384/58-1 from the Deutsche Forschungsgemeinschaft (DFG) and from the Helmholtz Association (NACIP program). Dr. X.H. Peng thanks Arizona State University Advanced Computing Center for providing computing resources (Agave Cluster). S.M. thanks Dr. V. Aravindan for providing the facilities for electrochemical measurements and Akshay Manohar V. for the EDX measurements, Dr. Jason Tresback, Center for Nanoscale, School of Engineering and Applied Sciences, SEAS, Harvard University for AFM images, Dr. Somu Sivasubramanian, Northeastern University for SEM images and Vijayamohan would like to thank SERB for the J.C. Bose Fellowship (JCB/2020/000018). Raman studies are partially supported by funds from the National Institutes of Health (Grants to R.P.: R01CA209888 and R21EB022298) and NIH 5P41EB015871.



View Article Online
DOI: 10.1039/D4YA00217B

Open Access Article. Published on 21 6 2024. Downloaded on 2024-07-07 9:07:45.
This article is licensed under a Creative Commons Attribution-NonCommercial 3.0 Unported Licence.



Energy Advances Accepted Manuscript

Author Contributions:

Sneha Mandal: Electrochemical studies, data analysis, manuscript first drafting

Vijayamohanan Pillai: Electrochemical studies, drafting and reviewing

Mano Ranjana Ponraj: Data analysis, results validations, drafting

Thushara K M: Material synthesis and characterization, manuscript drafting

Jebasingh Bhagavathsingh: Conceptualization, funding, drafting, reviewing

Stephan L Grage: ^{13}C , ^7Li and ^6Li solid state MAS NMR studies

Xihong Peng: Density functional theory of intercalated GO

Jeon Woog Kang: Raman studies

Dorian Liepmann: Raman analysis

Arunachala Mada Kannan: Electrochemical experimental design, analysis and reviewing

Thavasi Velmurugan: Result analysis, draft corrections

Renugopalakrishnan Venkatasen: SEM, AFM, Raman. Conceptualizing Li^+ encapsulation in GO and reviewing.

Conflict of Interest: The authors are not involved in conflict of interest.



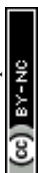
Reference

View Article Online
DOI: 10.1039/D4YA00217B

1. Armand, M., Tarascon, J. M. Building better batteries. *Nature*, 2008, **451**, 652–657.
2. Grey, C.P., Hall, D.S. Prospects for lithium-ion batteries and beyond—a 2030 vision. *Nat Commun.*, 2020, **11**, 6279–6283.
3. Liu, S., Kang, L., and Jun, S., C. Challenges and Strategies toward Cathode Materials for Rechargeable Potassium-Ion Batteries. *Adv. Mater.*, 2021, **33**, 2004689.
4. Liu, S., Kang, L., Henzie, J., Zhang, J., Ha, J., Amin, M. A., Hossain, M. S. A., Jun, S. C., and Yamauchi, Y. Recent Advances and Perspectives of Battery-Type Anode Materials for Potassium Ion Storage. *ACS Nano*, 2021, **15**, 18931–18973.
5. Abakumov, A.M., Fedotov, S.S., Antipov, E.V. Solid state chemistry for developing better metal-ion batteries. *Nat. Commun.*, 2020, **11**, 4976–4980.
6. Easley et al., Imagining circular beyond lithium-ion batteries, *Joule*, 2022, <https://doi.org/10.1016/j.joule.2022.06.022>.
7. A. M. Kannan, V. Renugopalakrishnan, S. Filipek, P. Li, G. F. Audette, and L. Munukutla. Bio-Batteries and Bio-Fuel Cells: Leveraging on Electronic Charge Transfer Proteins. *J. Nanosci. Nanotechnol.*, 2009, **9**, 3, 1665–1678.
8. Rachid Essehli, Anand Parejiya, Nitin Muralidharan, Charl J. Jafta, Ruhul Amin, Marm B. Dixit, Yaocai Bai, Jue Liu c, Ilias Belharouak. Hydrothermal synthesis of Co-free NMA cathodes for high performance Li-ion batteries. *J. Power Sources*, 2022, **545**, 231938
9. Lin, D., Liu, Y. Cui, Y. Reviving the lithium metal anode for high-energy batteries. *Nature Nanotech.*, 2017, **12**, 194–206.
10. Chan, C.K. Zhang, X.F. and Cui, Y. High Capacity Li-ion Battery Anodes Using Ge Nanowires. *Nano Lett.*, 2008, **8**, 1, 307–309.



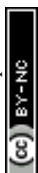
11. Hui Wu, Yi Cui. Designing nanostructured Si anodes for high-energy lithium-ion batteries. *Nano Today*, 2012, 7, 414-429. View Article Online
DOI: 10.1039/D1TA00217B
12. Yin, J. Cao, H. Zhou, Z. Zhang, J. and Qu, M. SnS₂@reduced graphene oxide nanocomposites as anode materials with high capacity for rechargeable lithium-ion batteries. *J. Mater. Chem.*, 2012, 22, 2396 -23970.
13. Zhou, X. Wan, L. J. and Guo, Y. G. Binding SnO₂ Nanocrystals in Nitrogen-Doped Graphene Sheets as Anode Materials for Lithium-Ion Batteries. *Adv. Mater.*, 2013, 25, 2152–2157.
14. Ji, K., Han, J., Hirata, A. *et al.* Lithium intercalation into bilayer graphene. *Nat Commun.*, 2019, 10, 275-285.
15. Zhang, J. Cao, H. Tang, X. Fan, W. Peng, G. Qu, M. Graphite/graphene oxide composite as high capacity and binder-free anode material for lithium ion batteries. *Journal of Power Sources*, 2013, 241, 619-626.
16. Raccichini, R., Varzi, A., Passerini, S. *et al.* The role of graphene for electrochemical energy storage. *Nature Mater.*, 2015, 14, 271–279.
17. Francesco Bonaccorso, Luigi Colombo, Guihua Yu, Meryl Stoller, Valentina Tozzini, Andrea C. Ferrari, Rodney S. Ruoff, Vittorio Pellegrini. Graphene, related two-dimensional crystals, and hybrid systems for energy conversion and storage. *Science*, 2015, 347, 1246501-1246508.
18. Soroosh Sharifi-Asl, Fernando A. Soto, Tara Foroozan, Mohammad Asadi, Yifei Yuan, Ramasubramonian Deivanayagam, Ramin Rojaee, Boao Song, Xuanxuan Bi, Khalil Amine, Jun Lu, Amin Salehi-khojin, Perla B. Balbuena, and Reza Shahbazian-Yassar. Anti-Oxygen Leaking LiCoO₂. *Adv. Funct. Mater.*, 2019, 1901110- 1901121.



19. Cheng J. Sun, M. Sadd, P. Edenborg, H. Grönbeck, P. H. Thiesen, Z. Xia, V. Quintano, R. Qiu, A. Matic, V. Palermo, Real-time imaging of Na⁺ reversible intercalation in “Janus” graphene stacks for battery applications. *Sci. Adv.*, 2021, 7, eabf0812. View Article Online
DOI:10.1039/D1AA00217B
20. Isaac, B. R., Alwarappan, S. and Pillai, V. K. Van der Waals Gap Engineering of Multiwalled Carbon Nanotubes in Ionic Liquids at Room Temperature. *ACS Sustainable Chem. Eng.*, 2023, 11, 46, 16641–16649.
21. Zhang, J., Li, C., Peng, Z. 3D free-standing nitrogen-doped reduced graphene oxide aerogel as anode material for sodium ion batteries with enhanced sodium storage. *Sci Rep.*, 2017, 7, 4886-4893
22. Na Li, Zongping Chen, Wencai Ren, Feng Li, and Hui-Ming. Flexible graphene-based lithium-ion batteries with ultrafast charge and discharge rates. *PNAS*, 2012, 109(43) 17360–17365.
23. Radich, E.J. and Kamat, P.V. Origin of Reduced Graphene Oxide Enhancements in Electrochemical Energy Storage. *ACS Catal.*, 2012, 2, 807–816.
24. Stankovich, S. Dikin, D.A. Richard D. Piner, Kevin A. Kohlhaas, Alfred Kleinhammes, Yuanyuan Jia, Yue Wu, SonBinh T. Nguyen b, Rodney S. Ruoff. Synthesis of graphene-based nanosheets via chemical reduction of exfoliated graphite oxide. *Carbon*, 2007, 45, 1558–1565.
25. Yige Sun, Jie Tang, Kun Zhang, Jinshi Yuan, Jing Li, Da-Ming Zhu, Kiyoshi Ozawa and Lu-Chang Qin. Comparison of reduction products from graphite oxide and graphene oxide for anode applications in lithium-ion batteries and sodium-ion batteries. *Nanoscale*, 2017, 9, 2585- 2595.
26. Kim, C. Cheong, J.Y. Kim, D. and Lee et al., An angstrom-level d-spacing control of graphite oxide using organofillers for high-rate lithium storage, *Chem* 2022, 8, 2393–2409,



27. Jiwon Jang, Seok Hyun Song, Hyeri Kim, Junsoo Moon, Hyungju Ahn, Kyoung-II Jo, Joon Bang, Hyungsub Kim, and Jaseung Koo. Janus Graphene Oxide Sheets with Fe₃O₄ Nanoparticles and Polydopamine as Anodes for Lithium-Ion Batteries. *ACS Appl. Mater. Interfaces*, 2021, 13, 14786–14795. New Article Online
DOI: 10.1039/D1TA00217B
28. Zhao, N., Song, P., Wen, H. *et al.* Graphene oxide grafting naphthoquinone derivative with enhanced specific capacitance and energy density for zinc-ion hybrid supercapacitors. *Ionics*, 2022, 28, 4425–4433.
29. Biradar, M.R., Rao, C. R. K., Bhosale, S. V., Bhosale, S. V. Bio-inspired adenine-benzoquinone-adenine pillar grafted graphene oxide materials with excellent cycle stability for high energy and power density supercapacitor applications. *Journal of Energy Storage*, 2023, 58, 106399.
30. Yue Gao, Daiwei Wang, Yun Kyung Shin, Zhifei Yan, Zhuo Han, Ke Wang, Md Jamil Hossain, Shuling Shen, Atif AlZahrani, Adri C. T. van Duin, Thomas E. Mallouk, and Donghai Wang. Stable metal anodes enabled by a labile organic molecule bonded to a reduced graphene oxide aerogel. *PNAS*, 2022, 117 (48) 30135-30141.
31. Banerjee, Moutusi; Gupta, Abhisek; Saha, Shyamal K.; Chakravorty, Dipankar. 1-Aza-15-Crown-5 Functionalized Graphene Oxide for 2D Graphene-Based Li⁺-ion Conductor. *Small*, 2015, 11(28), 3451–3457.
32. Abdollahifar, M. Doose, S. Cavers, H. and Kwade, A. Graphite Recycling from End-of-Life Lithium-Ion Batteries: Processes and Applications. *Adv. Mater. Technol.*, 2023, 8, 2200368-2200385.
33. Vasulinga, T.; Ravikumar, A. Convenient Large Scale Synthesis of *N*-BOC-Ethylenediamine. *Syn. Commun.*, 2006, 1767-1772 . Doi: 10.1080/00397919408010183.



34. Ramesh, P.; Jebasingh, B. Facile and effective oxidation of graphite using sodium metaperiodate. *Mat. Lett.*, 2017, 193, 305-308. DOI: 10.1016/j.matlet.2017.01.088.
35. Alexis Piñeiro-García, Sofia M. Vega-Díaz, Giovanni Mutton, Ferdinando Tristán, David Meneses-Rodríguez, and Vincent Semetey. Insights in the chemical composition of graphene oxide via a simple and versatile fluorescent labelling method. *ChemNanoMat*, 2021, 7, 842-850.
36. M. S. Dresselhaus, A. Jorio, M. Hofmann, G. Dresselhaus, R. Saito. Perspectives on Carbon Nanotubes and Graphene Raman Spectroscopy. *Nano Lett.*, 2010, 10, 3, 751–758. <https://doi.org/10.1021/nl904286r>.
37. E.J. Yoo, J. Kim, E. Hosono, H. Zhou, T. Kudo, I. Honma. Large Reversible Li Storage of Graphene Nanosheet Families for Use in Rechargeable Lithium-Ion Batteries. *NANO LETTERS*, 2008, 8, 8, 2277-2282.
38. Sergi Claramunt Aïda Varea David López-Díaz , M. Mercedes Velázquez Albert Cornet and Albert Cirera, The Importance of Interbands on the Interpretation of the Raman Spectrum of Graphene Oxide. *J. Phys. Chem. C*, 2015, 119, 10123–10129.
39. E. Pollak, B. Geng, K.J. Jeon, I. T. Lucas, T. J. Richardson, F. Wang, R. Kostecki, The Interaction of Li⁺ with Single-Layer and Few-Layer Graphene. *Nano Lett.*, 2010, 10, 9, 3386–3388.
40. A.S. Mazur, M.A. Vovk, P.M. Tolstoy. Solid-state ¹³C NMR of carbon nanostructures (milled graphite, graphene, carbon nanotubes, nanodiamonds, fullerenes) in 2000-2019: a mini-review. *Fullerenes, Nanotubes and Carbon Nanostructures*, 2020, 28, 202-213.
41. N. Li, D. Su. In-situ structural characterizations of electrochemical intercalation of graphite compounds. *Carbon Energy*, 2019, 1, 200-218.



42. K.J. Harris, Z.E.M. Reeve, D. Wang, X. Li, X. Sun, G.R. Goward. Electrochemical changes in lithium-battery electrodes studied using ^7Li NMR and enhanced ^{13}C NMR of graphene and graphitic carbons. *Chem. Mater.*, 2015, 27, 3299-3305.
43. M. Letellier, F. Chevallier, F. Beguin. In-situ ^7Li NMR during lithium electrochemical insertion into graphite and a carbon/carbon composite. *J. Phys. Chem. Solids*, 2006, 67, 1228-1232.
44. T. Gullion, J. Schaefer. Rotational-echo double-resonance NMR. *J. Magn. Reson.*, 1989, 81, 196-200.
45. Kang, L., Liu, S., Zhang, Q., Zou, J., Ai, J., Qiao, D., Zhong, W., Liu, Y., Jun, S. C., Yamauchi, Y., and Zhang. J. Tensile Strain-Mediated Spinel Ferrites Enable Superior Oxygen Evolution Activity. *J. Am. Chem. Soc.*, 2023, 145, 24218–24229.
46. N. R. Wilson, P. A. Pandey, R. Beanland, R. J. Young, I. A. Kinloch, L. Gong, Z. Liu, K. Suenaga, J. P. Rourke, S. J. York, J. Sloan. Graphene Oxide: Structural Analysis and Application as a Highly Transparent Support for Electron Microscopy. *ACS Nano*, 2009, 3, 9, 2547–2556.
47. Stankovich, S. Piner, R. D. Nguyen, S. B. T. Ruof, R. S. Synthesis and exfoliation of isocyanate-treated graphene oxide nanoplatelets. *Carbon*, 2006, 44, 3342–3347.
48. Szirmai, P., Márkus, B.G., Chacón-Torres, J.C. Eckerlein, P. Edlthammer, K. Englert, J. M. Mundloch, U. Hirsch A. Hauke, F. Náfrádi, B. Forró, L. Kramberger, C. Pichler, T. & Simon, F. Characterizing the maximum number of layers in chemically exfoliated graphene. *Sci Rep.* 2019, 9, 19480.
49. Kohn, W. & Sham, L. J. Self-Consistent Equations Including Exchange and Correlation Effects. *Phys. Rev.*, 1965, 144, A1133.
50. Kresse, G. & Furthmuller, J. Efficient iterative schemes for ab initio total-energy calculations using a plane-wave basis set. *Phys. Rev. B*, 1996, 54, 11169.

View Article Online
DOI: 10.1039/D4TA00217B



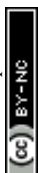
51. Kresse, G. & Furthmüller, J. Efficiency of ab-initio total energy calculations for metals and semiconductors using a plane-wave basis set. *Comput. Mater. Sci.*, 1996, **6**, 15.
52. Blöchl, P. E. Projector augmented-wave method. *Phys. Rev. B*, 1994, **50**, 17953–17979
53. Kresse, G. & Joubert, D. From ultrasoft pseudopotentials to the projector augmented-wave method. *Phys. Rev. B*, 1999, **59**, 1758.
54. Perdew, J. P., Burke, K. & Ernzerhof, M. Generalized Gradient Approximation Made Simple. *Phys. Rev. Lett.*, 1996, **77**, 3865.
55. Grimme, S., Antony, J., Ehrlich, S. & Krieg, H. A consistent and accurate ab initio parametrization of density functional dispersion correction (DFT-D) for the 94 elements H-Pu. *J. Chem. Phys.*, 2010, **132**, 154104.
56. Monkhorst, H. J. & Pack, J. D. Special points for Brillouin-zone integrations. *Phys. Rev. B*, 1976, **13**, 5188–5192.
57. Aydinol, M. K. & Ceder, G. First-Principles Prediction of Insertion Potentials in Li-Mn Oxides for Secondary Li Batteries. *J. Electrochem. Soc.*, 1997, **144**, 3832–3835 (1997).
58. Aydinol, M. K., Kohan, A. F., Ceder, G., Cho, K. & Joannopoulos, J. Ab initio study of lithium intercalation in metal oxides and metal dichalcogenides. *Phys. Rev. B*, 1997, **56**, 1354–1365.
59. Sun, Y. Tang, J. Zhang, K. Yuan, J. Li, J. Zhu, D. M. Ozawa, K. and Qin, L. C. Comparison of reduction products from graphite oxide and graphene oxide for anode applications in lithium-ion batteries and sodium-ion batteries. *Nanoscale*, 2017, **9**, 2585-2595.
60. Kumar, A. Reddy, A. L. M. Mukherjee, A. Dubey, M. Zhan, X. Singh, N. Ci, L. Billups, W. E. Nagurny, J. Mital, G. and Ajayan, P. M. Direct Synthesis of Lithium-Intercalated Graphene for Electrochemical Energy Storage Application. *ACS Nano*, 2011, **5**, 6, 4345–4349.

View Article Online
DOI: 10.1039/D4TA00217B



61. Kornilov D, Penki TR, Cheglakov A, Aurbach D. Li/graphene oxide primary battery system and mechanism. *Battery Energy*. 2022;1:20210002.
62. Park, J.; Sharma, J.; Jafta, C.J.; He, L.; Meyer, H.M., III; Li, J.; Keum, J.K.; Nguyen, N.A.; Polizos, G. Reduced Graphene Oxide Aerogels with Functionalization-Mediated Disordered Stacking for Sodium-Ion Batteries. *Batteries*, 2022, 8, 12.
63. Zhao, C. Gao, H. Chen, C. and Wu, H. Reduction of graphene oxide in Li-ion batteries. *J. Mater. Chem. A*, 2015, 3, 18360 -18364.
64. Vivier, V. and Orazem, M. E. Impedance Analysis of Electrochemical Systems. *Chem. Rev.*, 2022, 122, 11131–11168.
65. Laschuk, N. O. Easton, E. B. and Zenkina, O. V. Reducing the resistance for the use of electrochemical impedance spectroscopy analysis in materials chemistry. *RSC Adv.*, 2021, 11, 27925-27936.
66. Obraztsov, I. Bakandritsos, A. Šedajová, V. Langer, R. Jakubec, P. Zoppellaro, G. Pykal, M. Presser, V. Otyepka, M. and Zbořil, R. Graphene Acid for Lithium-Ion Batteries—Carboxylation Boosts Storage Capacity in Graphene. *Adv. Energy Mater.*, 2022, 12, 2103010-2103020.
67. Ludwig, T., Je, M., Choi, H., Fischer, T., Roitsch, S., Müller, R., Mane, R. S., Kim, K. H., Mathur, S. Boosting nitrogen-doping and controlling interlayer spacing in pre-reduced graphene oxides. *Nano Energy*, 2020, 78 ,105286.
68. He, D. Xue, W. Zhao, R. Hu, W. Marsde, A. J. and Bissett, M. A. Reduced graphene oxide/Fe-phthalocyanine nanosphere cathodes for lithium-ion batteries. *J Mater Sci*, 2018, 53, 9170–9179.
69. Wang, Y. Li, X. Chen, L. Xiong, Z. Feng, J. Zhao, L. Wang, Z. Zhao, Y. Ultrahigh-capacity tetrahydroxybenzoquinone grafted graphene material as a novel anode for lithium-ion batteries. *Carbon*, 2019, 155, 445-452.

View Article Online
DOI:10.1039/D2TA00217B



70. Mondal, S., Ruidas S., Halankar, K. K., Mandal, B. P., Dalapati, S. and Bhaumik, A. A. metal-free reduced graphene oxide coupled covalent imine network as an anode material for lithium-ion batteries. *Energy Adv.*, 2020,1, 697–703. View Article Online
DOI: 10.1039/D4TA00217B
71. Meng, Y. Liu, X. Xiao, M. Hu, Q. Li, Y. Li, R. Ke, X. Ren, G. Zhu, F. Reduced graphene oxide@nitrogen doped carbon with enhanced electrochemical performance in lithium ion batteries. *Electrochimica Acta*, 2019, 309, 228-233.
72. Xu, Z., Yang, J., Hou, S., Lin, H., Chen, S., Wang, Q., Wei, H., Zhou, J., Zhuo, S. Thiophene-diketopyrrolopyrrole-based polymer derivatives/reduced graphene oxide composite materials as organic anode materials for lithium-ion batteries. *Chemical Engineering Journal*, 2022, 438, 135540.
73. Chen, P., Tao, W., Hu, M., Xu Y., Zhang, Z., Yu, H., Fu, X., Zhang, C. Boosting lithium storage by facile functionalization of graphene oxide nanosheets via 2-aminoanthraquinone. *Carbon*, 2021, 171 104-110.
74. Cahyadi, H. S. William, W. Verma, D. Kwak, S. K. and Kim, J. Enhanced Lithium Storage Capacity of a Tetralithium 1,2,4,5- Benzenetetracarboxylate (Li₄C₁₀H₂O₈) Salt Through Crystal Structure Transformation. *ACS Appl. Mater. Interfaces*, 2018, 10, 17183–17194.
75. Armand, M., Grugeon, S., Vezin, H. *et al.* Conjugated dicarboxylate anodes for Li-ion batteries. *Nature Mater.*, 2019, 8, 120–125.

